

A PHOTOMETRIC VARIABILITY SURVEY OF FIELD K AND M DWARF STARS WITH HATNET

J. D. HARTMAN¹, G. Á. BAKOS¹, R. W. NOYES¹, B. SÍPÓCZ^{1,2}, G. KOVÁCS³, T. MAZE⁴, A. SHPORER⁴, A. PÁL^{1,2}

Draft version October 25, 2018

ABSTRACT

Using light curves from the HATNet survey for transiting extrasolar planets we investigate the optical broad-band photometric variability of a sample of 27,560 field K and M dwarfs selected by color and proper-motion ($V - K \gtrsim 3.0$, $\mu > 30$ mas/yr, plus additional cuts in $J - H$ vs. $H - K_S$ and on the reduced proper motion). We search the light curves for periodic variations, and for large-amplitude, long-duration flare events. A total of 2120 stars exhibit potential variability, including 95 stars with eclipses and 60 stars with flares. Based on a visual inspection of these light curves and an automated blending classification, we select 1568 stars, including 78 eclipsing binaries, as secure variable star detections that are not obvious blends. We estimate that a further $\sim 26\%$ of these stars may be blends with fainter variables, though most of these blends are likely to be among the hotter stars in our sample. We find that only 38 of the 1568 stars, including 5 of the eclipsing binaries, have previously been identified as variables or are blended with previously identified variables. One of the newly identified eclipsing binaries is 1RXS J154727.5+450803, a known $P = 3.55$ day, late M-dwarf SB2 system, for which we derive preliminary estimates for the component masses and radii of $M_1 = M_2 = 0.258 \pm 0.008 M_\odot$ and $R_1 = R_2 = 0.289 \pm 0.007 R_\odot$. The radii of the component stars are larger than theoretical expectations if the system is older than ~ 200 Myr. The majority of the variables are heavily spotted BY Dra-type stars for which we determine rotation periods. Using this sample, we investigate the relations between period, color, age, and activity measures, including optical flaring, for K and M dwarfs, finding that many of the well-established relations for F, G and K dwarfs continue into the M dwarf regime. We find that the fraction of stars that are variable with peak-to-peak amplitudes greater than 0.01 mag increases exponentially with the $V - K_S$ color such that approximately half of field dwarfs in the solar neighborhood with $M \lesssim 0.2 M_\odot$ are variable at this level. Our data hints at a change in the rotation-activity-age connection for stars with $M \lesssim 0.25 M_\odot$.

Subject headings: stars: late-type, low-mass, rotation, flare, fundamental parameters (masses, radii)
 — binaries: eclipsing — surveys — catalogs — techniques: photometric

1. INTRODUCTION

Main-sequence stars smaller than the Sun are known to exhibit the following types of photometric variability: variability due to binarity (either eclipses or proximity effects such as ellipsoidal variability), variability due to the rotational modulation or temporal evolution of starspots, and flares. Below we discuss each type of variability, and what might be learned from studying it.

1.1. Low-Mass Eclipsing Binaries

Recent discoveries of eclipsing binaries (EBs) with K and M dwarf components have led to the realization that the radii of early M dwarfs and late K dwarfs are somewhat larger than predicted by theory (the number typically stated is 10%; Torres & Ribas 2002; Ribas 2003; López-Morales 2005; Ribas 2006; Beatty et al. 2007; Fernandez 2009). It has been suggested that the discrepancy between theory and observation for these binary star components may be due to their enhanced magnetic activity inhibiting convection. (Ribas 2006; Torres et al. 2006; López-Morales 2007; Chabrier et al. 2007). Support for this hypothesis comes from interferometric mea-

surements of the luminosity-radius relation for inactive single K and M dwarfs which appears to be in agreement with theoretical predictions (Demory et al. 2009). Testing this hypothesis will require finding additional binaries spanning a range of parameters (mass, rotation/orbital period, metallicity, etc.).

As transiting planets are discovered around smaller stars, the need for models that provide accurate masses and radii for these stars has become acute. For example, the errors in the planetary parameters for the transiting Super-Neptune GJ 436b appear to be dominated by the uncertainties in the stellar parameters of the $0.45 M_\odot$ M-dwarf host star (Torres 2007). Having a large sample of low mass stars with measured masses and radii would enable the determination of precise empirical relations between the parameters for these stars.

1.2. Stellar Rotation

The rotation period is a fundamental measurable property of a star. For F, G, K and early M main sequence stars there is a well-established relation between rotation, magnetic activity and age (e.g. Skumanich 1972; Noyes et al. 1984; Pizzolato et al. 2003). In addition to illuminating aspects of stellar physics, this relation in practice provides the best method for measuring the ages of field main sequence stars (Mamajek & Hillenbrand 2008; Barnes 2007).

For late M-dwarfs the picture is less clear. From a theo-

¹ Harvard-Smithsonian Center for Astrophysics, 60 Garden St., Cambridge, MA 02138, USA

² Department of Astronomy, Eötvös Loránd University, Budapest, Hungary.

³ Konkoly Observatory, Budapest, Hungary.

⁴ Wise Observatory, Tel Aviv University, Tel Aviv, Israel

retical standpoint one might expect that fully convective stars should not exhibit a rotation-activity connection if the connection is due to the $\alpha\Omega$ -dynamo process, which operates at the interface of the radiative and convective zones in a star, and is thought to generate the large scale magnetic fields in the Sun (see for example the discussion by Mohanty & Basri 2003). Nonetheless, several studies have found evidence that the rotation-activity connection may continue even to very late M-dwarfs (Delfosse et al. 1998; Mohanty & Basri 2003; Reiners & Basri 2007). In these studies the rotation period is inferred from the projected rotation velocity $v \sin i$, which is measured spectroscopically. Rotation studies of this sort suffer both from the inclination axis ambiguity, and from low sensitivity to slow rotation. Moreover, because low-mass stars are intrinsically faint, these studies require large telescopes to obtain high-resolution, high S/N spectra, so that typically only a few tens of stars are studied at a time.

There are two techniques that have been used to directly measure stellar rotation periods. The first technique, pioneered by Wilson & Bappu (1957), is to monitor the emission from the cores of the CaII H and K lines, searching for periodic variations. The Mount-Wilson Observatory HK project has used this technique to measure the rotation periods of more than 100 slowly rotating dwarfs and giant stars (Wilson 1978; Duncan et al. 1991; Baliunas et al. 1995, 1996). Alternatively, if a star has significant spot-coverage it may be possible to measure its rotation period by detecting quasi-periodic variations in its broad-band photometric brightness. Studies of this sort have been carried out in abundance for open clusters (e.g. Radick et al. 1987) as well as for some field stars (e.g. Strassmeier et al. 2000; Kiraga & Stepień 2007). While there are rich samples of rotation periods for K and M dwarfs in open clusters with ages $\lesssim 600$ Myr (Irwin et al. 2006, 2007, 2009a; Meibom et al. 2009; Hartman et al. 2009), the data for older K and M dwarfs is quite sparse. As such, there are few observational constraints on the rotational evolution of these stars after ~ 0.5 Gyr.

Given the existing uncertainties in the rotation-activity connection for low mass stars and the potential to use rotation as a proxy for age, a large, homogeneously collected sample of photometric rotation periods for field K and M dwarfs could potentially be of high value.

1.3. Flares

Flaring is known to be a common phenomenon among K and M dwarfs. Studies of open cluster and field flare stars have shown that the frequency of flaring increases with decreasing stellar mass, and decreases with increasing stellar age (e.g. Ambartsumyan et al. 1970; Mirzoyan et al. 1989). Significant flaring on these low-mass dwarfs is likely to impact the habitability of any planets they may harbor (e.g. Kasting et al. 1993; Lammer et al. 2007; Guinan & Engle 2009), so determining the frequency of flares, and its connection with other stellar properties such as rotation, has important implications for the study of exoplanets.

1.4. The HATNet Survey

To address these topics we use data from the Hungarian-made Automated Telescope Network (HAT-

Net; Bakos et al. 2004) and the Wise-HAT project (WHAT; Shporer et al. 2009) to conduct a variability survey of K and M dwarfs. The on-going HATNet project is a wide-field search for transiting extrasolar planets (TEPs) orbiting relatively bright stars. To date, the survey has announced the discovery of 26 TEPs, including HAT-P-11b (Bakos et al. 2009), one of only a handful of known transiting Super-Neptune planets. While the primary focus of the HATNet project has been the discovery of TEPs, some results not related to planets have also been presented. This includes studies of low-mass stars in single-lined eclipsing binary systems (Beatty et al. 2007; Fernandez 2009), as well as searches for variable stars (Hartman et al. 2004; Shporer et al. 2007).

1.5. Overview of the Paper

The structure of the paper is as follows. In § 2 we describe the HATNet photometric data, and select the sample of field K and M dwarfs. In § 3 we discuss our methods for selecting variable stars. We estimate the degree of blending for potential variables in § 4. We match our catalog of variables to other catalogs in § 5. We discuss the properties of the variables in § 6 including an analysis of one of the EB systems found in the survey. We conclude in § 7. In appendix A we present the catalog of variable stars.

2. OBSERVATIONAL DATA

2.1. HATNet Data

The HATNet project, which has been in operation since 2003, uses a network of 6 small (11 cm aperture), autonomous telescopes to obtain time-series observations of stars. The telescopes are distributed in longitude, with 4 in Arizona at Fred Lawrence Whipple Observatory (FLWO), and 2 in Hawaii on the roof of the Sub-Millimeter Array at Mauna Kea Observatory (MK). An additional seventh telescope, known as WHAT, is located at Wise Observatory in Israel and is identical in design to the HATNet telescopes. For details on the system design and observing procedure see Bakos et al. (2004, 2006); here we briefly review a few points that are relevant to the survey presented in this paper.

The HATNet telescopes have a fast focal ratio of $f/1.8$ yielding a plate-scale of $1031.315'' \text{ mm}^{-1}$. Prior to 2007 September each telescope employed a $2\text{K} \times 2\text{K}$ CCD and a Cousins I_C filter (Cousins 1976). The $2\text{K} \times 2\text{K}$ CCDs covered an $8.2^\circ \times 8.2^\circ$ field of view (FOV) at a pixel scale of $14''$. With these CCDs, stars with $7.5 \lesssim I_C \lesssim 14.0$ were observed with 5 minute exposures yielding a typical per-image photometric precision of a few mmag at the bright end, 0.01 mag at $I_C \sim 11$, and 0.1 mag at $I_C \sim 13.5$. After this date the telescopes were refitted with $4\text{K} \times 4\text{K}$ CCDs and Cousins R_C filters. The new CCDs cover a $10.6^\circ \times 10.6^\circ$ FOV at a pixel scale of $9''$. With these CCDs, stars with $8.0 \lesssim R_C \lesssim 15.0$ are observed with 5 minute exposures yielding a typical per-image photometric precision of a few mmag at the bright end, 0.01 mag at $R_C \sim 12$, and 0.1 mag at $R_C \sim 15$. The exact magnitude limits and precision per exposure as a function of magnitude vary within a field due to vignetting, and from field to field due to differences in the reduction procedure used (which has evolved over time) and in the degree of stellar crowding. In 2008 September the filters

were changed to Sloan r , though we do not include any observations taken through the new filters in the survey presented here. For both CCD formats, the typical full width at half maximum (FWHM) of the point spread function (PSF) is ~ 2 pixels (i.e. $\sim 30''$ for the 2K fields and $\sim 20''$ for the 4K fields).

The typical observing procedure is to assign to each telescope one to three fields to monitor, with several fields assigned concurrently to a telescope at MK and a telescope at FLWO. These fields are defined by dividing the sky into $838\ 7.5^\circ \times 7.5^\circ$ tiles. Each field is continuously observed at a cadence of 5.5 minutes for as long as it is visible (typically meaning the airmass is less than 2.0), or until another higher priority field rises. The total time spanned by the observations for a given field varies from 45 days to 2.5 years, with a median time span of half a year. The total number of exposures obtained for a given field varies from 1600 to 11,600 with a median value of 4800.

The data for this survey comes from 72 HATNet fields with declinations between $+15^\circ$ and $+52^\circ$. The survey covers approximately 4000 square degrees, or roughly 10% of the sky.

Both aperture photometry (AP) and image subtraction photometry (ISM) have been used for reductions. Both pipelines were developed from scratch for HATNet. See Pál (2009) for detailed descriptions of both methods (see also Bakos et al. 2004).

For both pipelines the Two Micron All-Sky Survey (2MASS; Skrutskie et al. 2006) is used as the astrometric reference. The astrometric solutions for the images are determined using the methods described by Pál & Bakos (2006) and Pál (2009). Photometry is performed at the positions of 2MASS sources transformed to the image coordinate system. For each resulting light curve the median magnitude is fixed to the I_C or R_C magnitude of the source based on a transformation from the 2MASS J, H and K_S magnitudes. We used the transformations:

$$R_C = 0.0606 + 2.7823J + 0.8922H - 2.6713K_S \quad (1)$$

$$I_C = 0.0560 + 2.0812J + 0.4074H - 1.4889K_S \quad (2)$$

which were determined from 590 Landolt standard stars (Landolt 1992) with 2MASS photometry. The RMS scatter of the residuals for these relations are 0.11 mag and 0.06 mag respectively. For the ISM reduction this magnitude is also used as the reference magnitude for each source in converting differential flux measurements into magnitudes. For each source, photometry is performed using three separate apertures. The set of apertures used has changed over time; the most recent reductions use aperture radii of 1.45, 1.95 and 2.35 pixels, which we have found to give light curves with the lowest RMS for both the 2K and 4K era observations, older observations which have not yet been re-reduced use aperture radii of 2.10, 2.55 and 3.20 pixels. Following the post-processing routines discussed below, we adopt a single “best” aperture for each light curve.

Both the AP and ISM pipelines produce light curves that are calibrated against ensemble variations in the flux scale. For ISM this is an automatic result of the method (see section 2.9 of Pál 2009). To select the photometric reference for the ISM method we manually choose an image from the set of images with the narrowest, but

not distorted, PSF, which were observed at low airmass on photometric nights with little background light from the Moon, and with the Sun well below the horizon. For AP the calibration is done using the method described in section 2.7.3 of Pál (2009). Briefly, for the AP pipeline a master reference image is selected by hand from a photometric night, and the magnitude transformation from each observed image to the reference image is fit for using a function that consists of a fourth order polynomial in the spatial coordinates and a linear dependence on the 2MASS $J - K_S$ color. After obtaining initial light curves for the stars the transformation is then redetermined this time rejecting stars that are outliers in the magnitude-RMS relation from the fit and weighting each star by the scatter of its light curve. Finally we reject images for which a substantial fraction of the transformed magnitudes are 3σ outliers in their respective light curves. Note that for fields observed by multiple telescopes the above procedure is performed on the combined set of observations. Following this procedure, the typical RMS of the light curves of the brightest non-saturated stars in a frame is ~ 5 mmag.

The calibrated light curves for each aperture are then passed through two routines that filter systematic variations from the light curves that are not corrected in calibrating the ensemble. The first routine (EPD) decorrelates each light curve against a set of external parameters including parameters describing the shape of the PSF, the sub-pixel position of the star on the image, the zenith angle, the hour angle, the local sky background, and the variance of the background (see Bakos et al. 2009; Pál 2009). For fields including observations from multiple telescopes the decorrelation is done independently on the data from each telescope. This procedure is applied assuming that each star has a constant magnitude. As discussed below, for large amplitude variable stars this will distort the signal and may lower the S/N of the detection, however such large amplitude variables will generally still be detectable, as confirmed by injecting sinusoid signals into raw light curves and attempting to recover them after applying the EPD procedure.

After applying EPD, the light curves are then processed with the Trend-Filtering Algorithm (TFA; Kovács, Bakos & Noyes 2005; Pál 2009) which decorrelates each light curve against a representative sample of other light curves from the field. The number of template light curves used differs between the fields, typically the number is $\sim 8\%$ of the total number of images for that field. In applying the TFA routine we also perform σ -clipping on the light curves since this generally reduces the number of false alarms when searching for transits. For the remainder of the paper we will refer to light curves that have been processed through EPD only, without application of TFA, as EPD light curves, and will refer to light curves that have been processed through both EPD and TFA as TFA light curves. We note that for some fields the EPD light curves were not stored and only TFA light curves are available.

Both of these algorithms tend to improve the signal to noise ratio of transit signals or low amplitude variations in the light curves, but they may distort the light curves of stars that show large-amplitude, long-period, continuous variability. Additionally the decorrelation against the zenith and hour angles in the EPD routine will tend

to filter out real variable star signals with periods very close to a sidereal day or an integer multiple of a sidereal day. Since these variables would be difficult to distinguish from systematic errors in the photometry, losing them from the sample may be unavoidable. The TFA routine in particular can distort long-period signals while improving the signal to noise ratio of short-period signals. For this reason we analyze both the EPD and TFA light curves, when available, to select variable stars (§ 3). We note that for the analysis in this paper we do not use the signal-reconstruction mode TFA presented by Kovács, Bakos & Noyes (2005). Once a signal is detected, TFA can be run in this mode to obtain a trend-filtered light curve that is free of signal distortions, however for signal detection one must use zero-signal TFA since the signal is not known a priori.

Finally, an optimal aperture is chosen for each star. For stars fainter than a fixed limit the smallest aperture is used (to minimize the sky noise), for brighter stars the aperture with the smallest root-mean-square (RMS) light curve is used.

2.2. Composite Light Curves

Because the separation between the HATNet field centers is smaller than the FOV of the HATNet telescopes for both the 2K and 4K CCDs, some stars are observed in multiple fields. These stars may have more than one light curve, which we combine into composite light curves. In making a composite light curve we subtract the median magnitude from each component light curve. For fields reduced with both ISM and AP we use the light curve with the lowest RMS, and in the case of equal RMS we use the ISM light curve. Note that the composite light curve for a star may include a mix of I_C and R_C photometry. While the amplitude of variability may be different from filter to filter, the period and phasing for variations due to eclipses or the rotational modulation of starspots will be independent of bandpass.

We do not allow for independent amplitudes of different filters in searching for variability using the methods described in § 3. To verify that this does not significantly affect the detection of periodic signals, we injected sinusoids with periods between 0.1 and 100 days drawn from a uniform logarithmic distribution, and amplitudes between 0.01 and 1.0 mag taken from a uniform logarithmic distribution into the light curves of 553 non-variable stars which have both I_C and R_C photometry. We adopted independent amplitudes for the I_C and R_C light curves of a given star, but adopted the same phase and period for the variations. We then attempted to recover the injected signals in the combined light curves using the AoVHarm technique discussed in § 3. We find that in 99% of the cases the peak frequency found in the AoVHarm periodogram is within $1/T$ of the injected frequency, where T is the timespan of the composite light curve. We also performed the simulations allowing the I_C and R_C light curves to have independent phases as well as independent amplitudes, and find that the recovered period agrees with the injected period in 96% of the cases. We note that this simple merging of photometry from different filters may result in spurious side lobes in the power spectrum, so for a more detailed analysis of individual objects, including searches for multiple frequencies of variation, this effect should be considered.

2.3. Selection of the K and M Dwarf Sample

Combining photometric observations with proper motion measurements is an effective method for selecting nearby dwarf stars. This technique is routinely used in the search for cool stars in the solar neighborhood (e.g. Reyle & Robin 2004), and has been suggested as an effective method for screening giants from transit surveys (Gould & Morgan 2003).

To select our sample of stars that are probable K and M dwarfs we apply cuts on the proper motion and on the color. Proper motion measurements are taken from the PPM-Extended catalog (PPMX; Röser et al. 2008) which provides proper motions with precisions ranging from 2 mas/yr to 10 mas/yr for 18 million stars over the full sky down to a limiting magnitude of $V \sim 15.2$. The PPMX catalog provides complete coverage of the HATNet survey for stars with $V - I_C \lesssim 1.2$ for the 2K fields and for stars with $V - R \lesssim 0.7$ for the 4K fields. For stars redder than these limits, the faint limit of HATNet is deeper than the faint limit of PPMX. We select all stars from this catalog with a proper motion $\mu > 30$ mas/yr, as these are stars for which the proper motion is detected with better than 3σ confidence. For the color selection we use the 2MASS JHK_S photometry and, where available, V -band photometry from the PPMX catalog, which is taken from the Tycho-2 catalog (Høg et al. 2000) and transformed to the Johnson system by Kharchenko (2001). Only $\sim 4\%$ of the stars have V photometry given in the PPMX catalog, for the majority of stars that do not have V photometry we calculate an initial approximate V magnitude using

$$V = -0.0053 + 3.5326J + 1.3141H - 3.8331K_S \quad (3)$$

which is determined from 590 Landolt Standard stars (Landolt 1992) with 2MASS photometry, and is used internally by the HATNet project to estimate the V magnitudes of transit candidates for follow-up observations. We then select stars with $V - K_S > 3.0$ which corresponds roughly to stars with spectral types later than K6 (Bessell & Brett 1988). This selects a total of 471,970 stars from the PPMX catalog, of which 33,177 fall in a reduced HATNet field; of these 32,831 have a HATNet light curve containing more than 1000 points.

Extrapolating a V magnitude from near-infrared photometry is not generally reliable to more than a few tenths of a magnitude. We therefore also obtained V magnitudes for stars in our sample by matching to the USNO-B1.0 catalog (Monet et al. 2003). This matching was done after the variability search described in § 3; we choose not to redo the sample selection and the subsequent variability selection. Note that low-mass subdwarfs, which have anomalously blue $V - K_S$ values, will pass a selection on $V - K_S > 3.0$ computed using eq. 3 to extrapolate the V magnitude, while they would not necessarily pass a selection using the measured value of $V - K_S$. To transform from the photographic B_U , R_U magnitudes in the USNO-B1.0 catalog to the V -band we use a relation of the form:

$$V = aB_U + bB_U^2 + cR_U + dR_U^2 + eB_U R_U + f \quad (4)$$

with coefficients given separately in table 1 for the $(B_{U,1}, R_{U,1})$, $(B_{U,1}, R_{U,2})$, $(B_{U,2}, R_{U,1})$ and $(B_{U,2}, R_{U,2})$ combinations, where $B_{U,1}$ and $B_{U,2}$ are the first and sec-

ond epoch blue photographic magnitudes respectively, and $R_{U,1}$ and $R_{U,2}$ are the first and second epoch red photographic magnitudes. These transformations were determined using ~ 1100 stars with both V photometry in the PPMX catalog and USNO-B1.0 (B_U, R_U) photometry. Based on the root-mean-square (RMS) scatter of the post-transformation residuals, we used the $(B_{U,2}, R_{U,2})$, $(B_{U,1}, R_{U,2})$, $(B_{U,2}, R_{U,1})$ and $(B_{U,1}, R_{U,1})$ transformations in order of preference. For stars with neither PPMX V photometry nor USNO-B1.0 photometry, we used eq. 3. For the remainder of the analysis in this paper, the V magnitude is taken from PPMX (Tycho-2) for 3.1% of the stars in our sample, from USNO-B1.0 for 93.6% of the stars, and is transformed from the 2MASS magnitudes for 3.3% of the stars.

Figure 1 shows the $J - H$ vs. $H - K_S$ color-color diagram for the selected sample. We also show the expected relations for dwarf stars and for giants. The relation for dwarfs is taken from a combination of the Baraffe et al. (1998) 1.0 Gyr isochrone for solar metallicity stars with $0.15 M_\odot \leq M \leq 0.7 M_\odot$ and the Chabrier et al. (2000) models for objects with $M \leq 0.075 M_\odot$. The JHK magnitudes for these isochrones were transformed from the CIT system (Elias et al. 1982, 1983) to the 2MASS system using the transformations determined by Carpenter (2001). The relation for giant stars with $\log g < 2.0$ is taken from the 1.0 Gyr, solar metallicity Padova isochrone (Marigo et al. 2008; Bonatto, Bica & Girardi 2004)⁵. While the majority of stars lie in the expected dwarf range, a significant number of stars fall along the giant branch. Some of these stars may be rare carbon dwarfs, but the majority are most likely giants with inaccurate proper motion measurements in the PPMX catalog. Of the 2445 selected stars with $J - H > 0.8$ that have HATNet light curves, 87% have undetected proper motions or proper motions less than 10 mas/yr in the USNO-B1.0 catalog, this is compared to 28% of the sample with $J - H < 0.8$. We note that the PPMX and USNO-B1.0 proper motions agree to within 20% for $\sim 62\%$ of the stars with $J - H < 0.8$ and which have proper motions given in USNO-B1.0, and to within 50% for $\sim 86\%$ of these stars. A visual inspection of the POSS-I and POSS-II Digitized Sky Survey images for a number of the sources with $J - H > 0.8$ and $\mu > 100$ mas/yr revealed none with visually detectable proper motion, and in many cases the object consists of two close, comparably bright stars, for which misidentification of sources may be to blame for the spurious proper motion detection. This includes several stars where the PPMX and USNO-B1.0 proper motion values are comparable. We therefore apply an additional cut in the $J - H$ vs $H - K_S$ color-color diagram as shown in figure 1 to reduce the sample to 28,785 stars.

Figure 2 shows a $V - J$ vs. H_J reduced proper-motion (RPM; Luyten 1922) diagram for the sample. Here the RPM, H_J , is calculated as

$$H_J = J + 5 \log_{10}(\mu/1000) \quad (5)$$

and gives a rough measure of the absolute magnitude M_J of a star. We show roughly the lines separating main sequence dwarfs from sub-dwarfs and giants. In figure 3

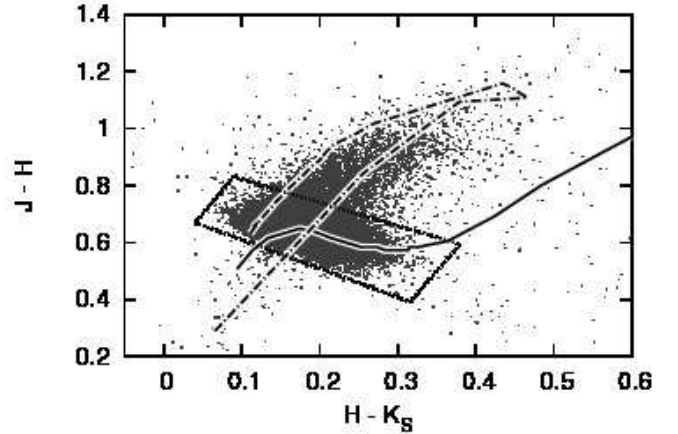


FIG. 1.— $J - H$ vs. $H - K_S$ color-color diagram for 32,831 stars that have $V - K_S > 3.0$ with V taken either from the PPMX catalog (Tycho-2) or extrapolated from the 2MASS J , H and K_S magnitudes using eq. 3, $\mu > 30$ mas/yr from the PPMX catalog, and that have a HATNet light curve containing more than 1000 points (gray-scale points). The solid line shows the expected relation for cool dwarfs (Baraffe et al. 1998; Chabrier et al. 2000), while the dot-dashed line shows the expected relation for giants (Marigo et al. 2008; Bonatto, Bica & Girardi 2004). Stars outside the area enclosed by the dotted line are rejected. For display purposes we have added slight Gaussian noise to the observed colors in the plot.

we compare the RPM to M_J for 239 stars in the sample which have a Hipparcos parallax (Perryman et al. 1997). To remove additional giants from the sample we reject 1225 stars with $H_J < 3.0$, leaving our final sample of 27,560 stars.

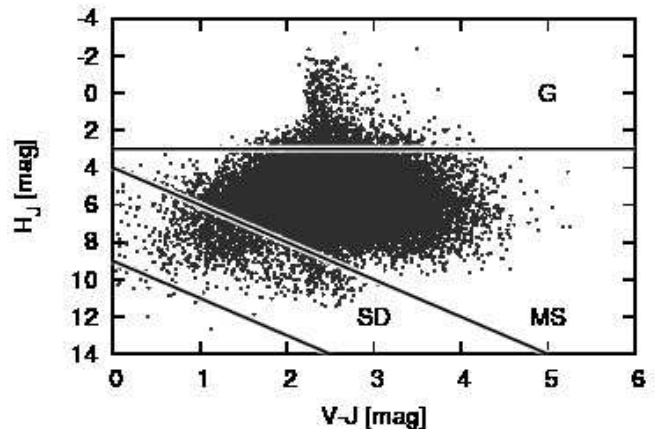


FIG. 2.— $V - J$ vs. H_J RPM diagram for stars with $\mu > 30$ mas/yr passing $V - K_S$ and JHK color cuts. Note that in this plot we use V magnitudes that are transformed from the USNO-B1.0 photographic magnitudes for the majority stars, and not the V magnitudes transformed from JHK that were used in applying the initial $V - K_S$ cut. The lines separate main sequence dwarfs from sub-dwarfs and giants. We reject the 1225 stars with $H_J < 3.0$. The lines separating main sequence dwarfs from sub-dwarfs are taken from Yong & Lambert (2003).

3. SELECTION OF VARIABLE STARS

To search for periodic variations we use the harmonic-fitting Analysis of Variance periodogram (AovHarm; Schwarzenberg-Czerny 1996) and the Box-Least-Squares

⁵ The isochrone was obtained from the CMD 2.1 web interface <http://stev.oapd.inaf.it/cgi-bin/cmd.2.1>

TABLE 1
COEFFICIENTS FOR TRANSFORMATIONS FROM USNO-B1.0 B_U AND R_U MAGNITUDES TO V (EQ. 4).

B_U	R_U	a	b	c	d	e	f	RMS [mag]
1	1	-0.76 ± 0.19	-0.02 ± 0.01	1.71 ± 0.15	-0.14 ± 0.01	0.15 ± 0.02	1.63 ± 0.52	0.27
1	2	0.72 ± 0.08	-0.061 ± 0.002	0.38 ± 0.06	-0.057 ± 0.006	0.114 ± 0.007	-0.89 ± 0.26	0.19
2	1	0.85 ± 0.09	-0.045 ± 0.006	0.44 ± 0.08	-0.051 ± 0.003	0.079 ± 0.008	-1.52 ± 0.24	0.22
2	2	0.73 ± 0.14	-0.164 ± 0.008	0.46 ± 0.13	-0.20 ± 0.01	0.35 ± 0.02	-0.75 ± 0.26	0.19

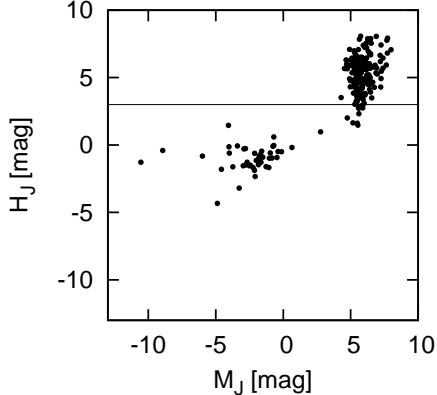


FIG. 3.— The absolute magnitude M_J vs. the RPM for 239 stars in the sample which have a Hipparcos parallax. This confirms that the RPM provides a rough estimate of the absolute magnitude for this sample of stars. We reject stars with $H_J < 3.0$, as these appear to be predominately giants.

(BLS; Kovács, Zucker & Mazeh 2002) algorithm as implemented in the VARTOOLS program⁶ (Hartman et al. 2008). We also conduct a search for flare-like events in the light curves. We apply the AoVHarm and BLS algorithms to both the EPD and TFA light curves of sources, when available. For the flare-search we use only the EPD light curves because the σ -clipping applied to the TFA light curves may remove real flares.

In addition to the searches mentioned above, we also tested the phase-binning AoV periodogram (AoV; Schwarzenberg-Czerny 1989), and the Discrete Auto-Correlation Function (DACF; Edelson & Krolik 1988) to search for periodic and quasi-periodic signals. We found that both of these techniques yield a substantial number of false alarm detections that must then be culled by eye (for the DACF technique more than half of the selected potential variables were determined to be false alarms during a visual inspection of the light curves), and only a relatively small number of detections that are visually judged to be robust and are not also selected by the AoVHarm technique. We therefore do not give further consideration to these methods.

In the following subsections we discuss the AoVHarm, BLS and flare searches in turn. The resulting catalog of variable stars is presented in appendix A.

3.1. Harmonic AoV

We run the AoVHarm algorithm (Schwarzenberg-Czerny 1996) on the full sample of stars. We first apply an iterative 5σ clipping to the

light curve before searching for periods between 0.1 and 100 days. We run the algorithm using a sinusoid model with no higher harmonics (it is thus comparable to DFT methods, or to the popular Lomb-Scargle technique; Lomb 1976; Scargle 1982), and generate the periodogram at a frequency resolution of $0.1/T$ where T is the total time-span covered by a given light curve. We then determine the peak at 10 times higher resolution. As our figure of merit we use the signal-to-noise ratio (S/N), with an iterative 5σ clipping applied to the periodogram in calculating the noise (the RMS of the periodogram).

To select the variables we group the light curves by the post-processing applied (EPD or TFA), the CCD format (2K or 4K) and the magnitude of the source. We adopt a separate selection threshold on S/N for each group. The thresholds have the form

$$S/N_{\min} = \begin{cases} S/N_0 & \text{if } P < P_0 \\ S/N_0 (P/P_0)^\alpha & \text{if } P \geq P_0 \end{cases} \quad (6)$$

The adopted values of S/N_0 range from 20-40, while the adopted values of α range from 0 to 0.5. We use $P_0 = 4$ days for all groups. To establish the false alarm probability associated with these S/N thresholds, we simulated white noise light curves with time sampling drawn randomly from the HATNet light curves, calculate the AoVHarm periodogram for each simulation, and determine the S/N of the highest peak in each periodogram using the same procedure as for the real light curves. We find that the false alarm probability (FAP) as a function of S/N is well fitted by a function of the form:

$$\text{FAP} = 1 - \left[1 - e^{-0.90(S/N+1)} \right]^{3350} \quad (7)$$

A cut-off at $S/N > 20$ thus corresponds to a FAP of $\sim 2 \times 10^{-5}$ while a cut-off at $S/N > 40$ corresponds to a FAP of $\sim 4 \times 10^{-13}$. The expected total number of false alarms for our sample of stars is thus fewer than 1. Figure 4 shows the AoVHarm S/N as a function of the peak period for various light curve groups. The adopted thresholds increase as a function of period to account for temporally correlated systematic errors in the photometry. In addition to this selection we also reject detections with periods near 1 sidereal day, one of its harmonics, or other periods which appear as spikes in the histogram of detected periods (the latter includes periods between 5.71 and 5.80 days). For composite light curves that contain both 2K and 4K observations we take

$$S/N_{\min} = f_{2K} S/N_{\min, 2K} + f_{4K} S/N_{\min, 4K} \quad (8)$$

where f_{2K} and f_{4K} are the fraction of points in the light curve that come from 2K and 4K observations, and

⁶ The VARTOOLS program is available at <http://www.cfa.harvard.edu/~jhartman/vartools/>

$S/N_{\min,2K}$ and $S/N_{\min,4K}$ are the 2K and 4K thresholds at the period of the composite light curve.

Our selection threshold passes a total of 1337 EPD light curves, and 1717 TFA light curves. These are inspected by eye to reject obvious false alarms and to identify EBs. There are 1082 EPD light curves that we judge to show clear, continuous, periodic variability, 34 that show eclipses, 185 that we consider to be questionable (these are included in the catalog, but flagged as questionable), and 36 that we reject. For the TFA light curves the respective numbers are 1443, 43, 217, and 14. Note that the distinction between “clear” variability and “questionable” cases is fairly subjective. Generally we require the variations to be obvious to the eye for periods $\gtrsim 30$ days, for shorter periods we consider the selection to be questionable if it appears that the variability selection may be due to enhanced scatter on a few nights.

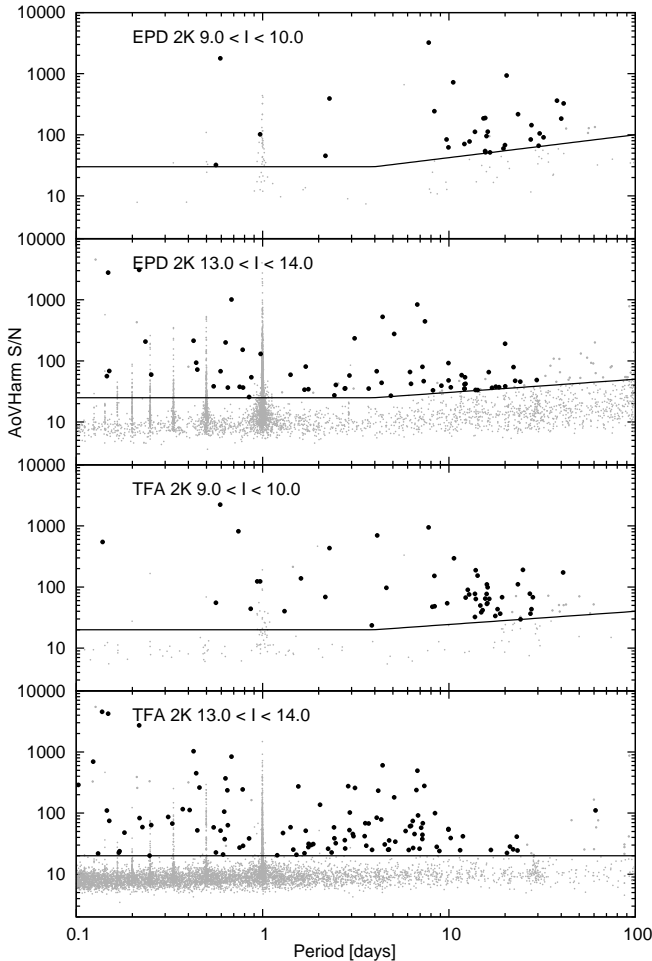


FIG. 4.— Period vs. S/N from AoVHarm for 4 representative light curve groups. We show the light curves that pass the automatic selection and are flagged as reliable detections during the by-eye inspection (dark filled points) and the light curves that do not pass the selection or are flagged as unreliable detections (grey filled points) separately. The lines show the adopted S/N cut-off as a function of period. Note that in addition to the cut-off shown with the line, we also automatically reject light curves for which the peak period is close to one sidereal day or a harmonic of one sidereal day.

3.2. BLS - Search for Eclipses

The BLS algorithm, primarily used in searches for transiting planets, detects periodic box-like dips in a light curve. This algorithm may be more sensitive to detached binaries with sharp-featured light curves than the other methods used. For our implementation of the BLS algorithm we search 9,000 evenly spaced frequency points covering a period range of 0.1 to 1.0 days and 100,000 evenly spaced frequency points covering a period range of 1.0 to 20.0 days. At each trial frequency we bin the phased light curve into 200 bins, and search over fractional eclipse durations ranging from 0.01 to 0.1 in phase. Figure 5 shows the S/N vs the period for the EPD and TFA light curves. We select 752 stars with $S/N > 10.0$ and with a period not close to 1 sidereal day or a harmonic of a sidereal day as potentially eclipsing systems. The selected light curves are inspected by eye to identify eclipsing systems. A total of 89 candidate EB systems are found in this manner, 8 are found in the EPD light curves only, 29 are found in the TFA light curves only, and 52 are found in both the EPD and TFA light curves.

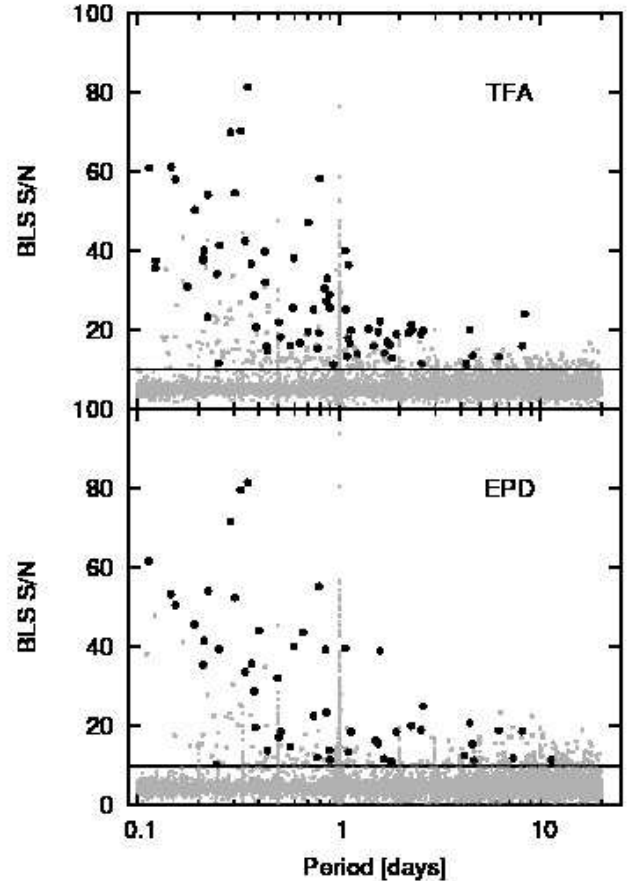


FIG. 5.— Period vs. S/N from BLS for EPD and TFA light curves. The dark points show light curves that pass the $S/N > 10.0$ cut, do not have a period near a sidereal day or one of its harmonics, and are selected as eclipsing binaries during the by eye inspection. The grey points show all other light curves.

3.3. Search for Flares

As noted in the introduction, flaring is a common phenomenon among K and M dwarfs. While we were inspecting the light curves of candidate variable stars we noticed a number of stars showing significant flares. We therefore decided to conduct a systematic search for flare events in the light curves. Most optical stellar flares show a very steep rise typically lasting from a few seconds to several minutes. Krautter (1996) notes that flares can be divided into two classes based on their decay times: “impulsive” flares have decay times of a few minutes, to a few tens of minutes, while “long-decay” flares have decay times of up to a few hours. Due to the 5-minute sampling of the HATNet light curves, flares of the former type will only affect one or two observations in a light curve, unless the peak-height is exceptionally large, while flares of the latter type might affect tens of observations. In general it is very difficult to determine whether a given outlier in a light curve is due to a flare or bad photometry without inspecting the images from which an observation was obtained. This is impractical to do for tens of thousands of light curves when each light curve may contain tens to hundreds of outliers. While observations that are potentially corrupted are flagged, in practice the automated routines that generate these flags do not catch all cases of bad photometry. We therefore do not attempt to identify individual “impulsive” flares affecting only a few points in the light curves. Long-decay flares, or very high-amplitude impulsive flares, on the other hand, may be searched for in an automated fashion if a functional form for the decay is assumed (this is similar to searching for microlensing events, see for example Nataf et al. 2009). To search for long-decay flares we used the following algorithm:

1. Compute m_0 , the median magnitude of the light curve, and δ_0 the median deviation from the median.
2. Identify all sets of consecutive points with $m - m_0 < -3\delta_0$. Let t_0 be the time of the brightest observation in a given set, and let N be the number of consecutive points following and including t_0 with $m - m_0 < -2\delta_0$. We proceed with the set if $N > 3$.
3. Use the Levenberg-Marquardt algorithm (Marquardt 1963) to fit to the N points a function of the form:

$$m(t) = -2.5 \log_{10} \left(A e^{-(t-t_0)/\tau} + 1 \right) + m_1 \quad (9)$$

where A , τ and m_1 are the free parameters. Here A is the peak intensity of the flare relative to the non-flaring intensity, τ is the decay timescale, and m_1 is the magnitude of the star before the flare. For the initial values we take $m_1 = m_0$, $\tau = 0.02$ days, and $A = 10^{-0.4(m_p - m_0)} - 1$, where m_p is the magnitude at the peak.

4. Perform an F-test (see Lupton 1993) on the statistic

$$f = \frac{(\chi_{N-1}^2 - \chi_{N-3}^2)/2}{\chi_{N-3}^2/(N-3)} \quad (10)$$

where χ_{N-1}^2 is the χ^2 value about the mean and χ_{N-3}^2 is the χ^2 value from fitting eq. 9. If the false

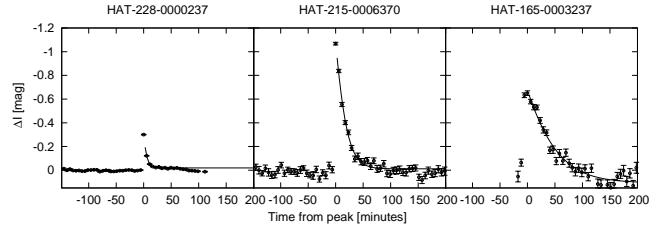


FIG. 6.— Three examples of flares seen in the HATNet light curves. In each case the solid line shows the fit of eq. 9 to the light curve.

alarm probability is greater than 1%, reject the candidate. If not, increase the number of points by one and repeat step 3. Continue as long as the false alarm probability decreases.

5. We reject any flare candidate for which there are at least two other candidate flares from light curves in the same field that occur within 0.1 days of the flare candidate.
6. Let the number of points with $t < t_0$ and $t_0 - t < 0.05$ days be N_{before} and the number of points with $t > t_1$ and $t - t_1 < 0.05$ days be N_{after} . Here t_1 is the time of the last observation included in the fit. Reject the candidate flare if $N_{\text{before}} < 2$ or $N_{\text{after}} < 2$. Also reject the candidate flare if $A < 0.$, $A > 10.0$, $\tau < 0.001$ days, $\tau > 0.5$ days, $A < \sigma_A$, $\tau < \sigma_\tau$, or if the false alarm probability from step 4 is greater than 0.1%. Here σ_A and σ_τ are the formal uncertainties on A and τ respectively. The selection on A is used to reject numerous light curves with significant outliers which appear to be due to artifacts in the data rather than flares.

We apply the above algorithm to the non-composite EPD light curves (i.e. light curves from each field are processed independently for stars with light curves from multiple fields). The algorithm is applied both on the raw EPD light curves, and on EPD light curves that are high-pass filtered by subtracting from each point the median of all points that are within 0.1 day of that point. There are a total of 23,589 stars with EPD light curves that are analyzed, we exclude from the analysis 3971 stars from the full sample for which only σ -clipped TFA light curves are available. A total of 320 candidate flare events from 281 stars are selected. These are inspected by eye to yield the final sample of 64 flare events from 60 stars. During the visual inspection we improved the automated fit for some of the flares by manually adjusting the range of points used in the fit. Figure 6 shows two examples of these large-amplitude, long-decay flares. The identified flares have peak intensities that range from $A = 0.07$ to $A = 4.21$ and decay time-scales that range from $\tau \sim 5$ minutes to $\tau \sim 1$ hour.

3.4. Independent Search for Periodic Variables in a Subset of the K/M Dwarf Sample

As a check on the reliability of our variable star detections, an independent selection of variables was conducted on a subset of the K/M dwarf sample. A total of 3187 light curves were analyzed from 7 different HATNet fields using the DFT-based method described by Szulágyi et al. (2009). The light curves were cleaned

of trends using 700 TFA template light curves for each field, and a polynomial is fit and subtracted from the DFT power spectrum for each light curve to further correct for red noise. Light curves with $S/N > 8$ were selected as variables. An iterative search for additional frequencies of variability was conducted on each of these light curves by successively fitting a Fourier series to the light curve and calculating the DFT power spectrum of the residual. Two examples of multiperiodic variables identified in this way are discussed in Section 6.4. A total of 4.6% of the analyzed light curves were selected by this method, 80% of these were also selected as variables by the AoVHarm method. On the other hand, 40% of the variables selected by AoVHarm applied to the TFA light curves from these fields were not selected by DFT. There are several factors which contribute to these differences, especially important are differences in the number of TFA templates used, in the adopted selection thresholds, in filtering applied to the power spectrum, and in the use of composite light curves (the DFT analysis did not use composite light curves for stars observed in more than one field). In general, TFA light curves with $AoVHarm\ S/N \gtrsim 100$ are selected by both the DFT and AoVHarm methods.

4. VARIABILITY BLENDING

While the wide FOV of the HATNet telescopes allows a significant number of bright stars to be simultaneously observed, the downside to this design is that the pixel scale is necessarily large, so a given light curve often includes flux contributions from many stars. Blending is a particularly significant issue in high stellar density fields near the Galactic plane. A star blended with a nearby variable star may be incorrectly identified as a variable based on its light curve. If the stars are separated by more than a pixel or two, it may be possible to distinguish the real variable from the blend by comparing the amplitudes of their light curves. However, because photometry is only obtained for stars down to a limiting magnitude (the value used varies from field to field), in many cases we do not have light curves for all the faint neighbors near a given candidate variable star, so we cannot easily determine which star is the true variable. In these cases we can still give an indication of whether or not a candidate is likely to be a blend by determining the expected flux contribution from all neighboring stars to the candidate's light curve.

4.1. Blending From Other Stars With Light Curves

To determine whether or not a candidate is blended with a nearby variable star that has a light curve, we measure the peak-to-peak light curve amplitude (in flux) of all stars within $2'$ of the candidate. If any neighbor has an amplitude that is greater than twice the flux amplitude of the candidate, the candidate is flagged as a probable blend. If any neighbor has an amplitude that is between half and twice the flux amplitude of the candidate, the candidate is flagged as a potential blend. If any neighbor has an amplitude that is between 10% and half the flux amplitude of the candidate, the candidate is flagged as an unlikely blend. And finally we flag the candidate as a non-blend if all neighbors have amplitudes that are less than 10% that of the candidate. We determine the amplitude of a light curve by fitting to it 10

different Fourier series of the form:

$$m(t) = m_0 + \sum_{i=1}^N a_i \sin(2\pi it/P + \phi_i) \quad (11)$$

with N ranging from 1 to 10. Here P is the period of the light curve. We perform an F-test to determine the significance of each fit relative to fitting a constant function to the light curve, and choose the amplitude of the Fourier series with the lowest false alarm probability. If the lowest false alarm probability is greater than 10% we set the amplitude to zero. We try all periods identified for each candidate by the variability searches described in § 3, and adopt the largest amplitude found. For candidates that have light curves from multiple fields, or that have both ISM and AP reductions, we do the amplitude test on each separate field/reduction and adopt the most significant blending flag found for the candidate. If the amplitude of the candidate variable star is set to zero for a given field/reduction we do not use that field/reduction in determining the blending flag. We use the EPD light curves in doing this test.

4.2. Blending From Faint Stars Without Light Curves

To determine whether or not a candidate is potentially blended with a nearby faint variable star that does not have a light curve, we compare the observed amplitude of the candidate to its expected amplitude if a neighboring star were variable with an intrinsic amplitude of 1.0 mag. We assume that an amplitude of 1.0 mag is roughly the maximum value that one might expect for a short period variable star. If the measured amplitude is less than the expected amplitude then we flag the candidate as a potential blend, if it is greater than the expected amplitude and less than twice the expected amplitude we flag the candidate as an unlikely blend, and if it is greater than twice the expected amplitude, we flag it as a non-blend. The test is done for all stars in the catalog (see the following subsection) within $2'$ of the candidate that do not have a light curve, and we adopt the most significant blending flag found for the candidate. To determine the expected amplitude of the candidate star induced by the neighbor, we note that a star with magnitude m_1 located near a variable star with magnitude m_2 and amplitude $\Delta m_2 > 0$, has an expected light curve amplitude that is given by

$$\begin{aligned} \Delta m_{1,AP} = & 2.5 \log_{10} \left[f_1 10^{-0.4m_1} + f_2 10^{-0.4(m_2 - \Delta m_2)} \right] \\ & - 2.5 \log_{10} \left[f_1 10^{-0.4m_1} + f_2 10^{-0.4m_2} \right] \end{aligned} \quad (12)$$

for the case of aperture photometry, and by

$$\begin{aligned} \Delta m_{1,ISM} = & 2.5 \log_{10} \left[f_1 10^{-0.4m_1} + f_2 10^{-0.4m_2} (10^{0.4\Delta m_2} - 1) \right] \\ & - 2.5 \log_{10} \left[f_1 10^{-0.4m_1} \right] \end{aligned} \quad (13)$$

for the case of image subtraction photometry. The two expressions differ because in the ISM pipeline photometry is done on difference images (only differential flux is summed in the aperture), whereas in the AP pipeline photometry is done directly on the science images (all stellar flux is summed in the aperture). Here $f_{1,2}$ is the fraction of the flux from star 1(2) that falls within the

aperture, and we use the catalog values (transformed in the case of 2MASS) for m_1 and m_2 . To determine f_1 and f_2 we integrate the intersection between the circular aperture and a Gaussian PSF which we assume to have a FWHM of 2 pixels (this is a typical effective “seeing” for both the 2K and 4K images), we do not consider pixelation effects in making this estimate.

4.3. Blending Results

We compare the results from the two blending tests for each candidate, and adopt the most significant blending flag from among the two tests for the catalog. We do not run the test on the candidate flare stars, unless the star was selected as a variable by another method as well.

We carried out this blending analysis twice: once using 2MASS for estimating the magnitudes of stars and identifying potentially contaminating neighbors, and a second time using the Sloan Digital Sky Survey Data Release 7 (SDSS DR7; Abazajian et al. 2009). The latter survey is deeper than 2MASS and also provides magnitudes in filters that are closer to those used by HATNet, however unlike 2MASS, SDSS DR7 does not provide complete coverage of the HATNet fields (43% of our stars have SDSS DR7 observations). We find that in the majority of cases (53%) the blending flags are the same when using SDSS or 2MASS to estimate the magnitudes of stars in the HATNet filters and to identify faint neighbors for which we have not obtained light curves. However, for a significant fraction (42%) the blending flag is higher when using SDSS than when using 2MASS. Typically the blending flag from SDSS is greater by one than the blending flag from 2MASS. We find that 6% of the objects are flagged as probable blends when using SDSS but unlikely blends when using 2MASS. To combine the results from 2MASS and SDSS for the analysis below we adopt the greater of the two blending flags, except for when there is no SDSS coverage, in which case we adopt the 2MASS blending flag. We report the 2MASS and SDSS blending flags separately in our catalogs.

Out of the 2095 stars that are selected as potential periodic variables, 507 are flagged as unblended, 340 are flagged as unlikely blends, 943 are flagged as potential blends, and 305 are flagged as probable blends.

As a consistency check on the blending classification scheme, we show in figure 7 the fraction of stars detected as variable as a function of the number of 2MASS sources within $30''$ of the star. The results are shown separately for stars with different blending classifications. The frequency of variability for stars not classified as probable blends does not increase with the number of neighbors, which shows the consistency of this method.

5. MATCH TO OTHER CATALOGS

5.1. Match to Other Variable Star Surveys

We match all 2120 stars selected as potential variables to the combined General Catalogue of Variable Stars (GCVS; Samus et al. 2006), the New Catalogue of Suspected Variable Stars (NSV; Kholopov 1982) and its supplement (NSVS; Kazarovets, Samus & Durlevich 1998)⁷. We also match to the ROTSE catalog of vari-

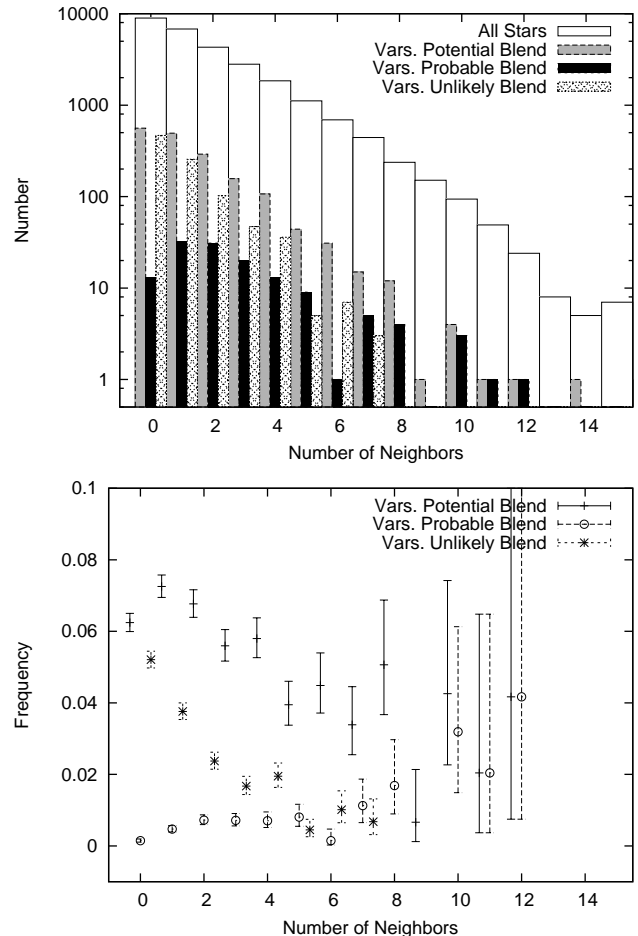


FIG. 7.— Top: The distribution of the number of stars within $30''$ of a given source shown for all stars in the sample, and for variable stars with different blending classifications. For the potential and unlikely blend groups we include all stars with that blending classification or a lesser blending classification. For the probable blend group we include only stars classified as probable blends. We only include variables classified by eye as reliable detections. Bottom: The fraction of all stars in the sample selected as variables using the same groups as in the top panel. The errorbars show the standard 1σ uncertainties from the binomial sampling distribution. The relative frequency of variability for stars not classified as probable blends does not increase for more crowded regions (it decreases due to increased photometric noise in more crowded regions), while the relative frequency of probable blends does increase for more crowded regions. This indicates that the blending classification scheme is consistent.

able stars (Akerlof et al. 2000), to the ALL Sky Automated Survey Catalogue of Variable Stars (ACVS; Pojmanski 2002)⁸, and to the Super-WASP catalogue of periodic variables coincident with ROSAT X-ray sources (Norton et al. 2007). In all cases we use a $2'$ matching radius. We use a large matching radius to include matches to known variables that may be blended with stars in our sample. In total 61 of our candidate variables lie within $2'$ of a source in one of these catalogs, meaning that 2059 are new identifications. This includes 29 that match to a source in the GCVS, 2 that match to a source in the NSV, 6 that match to a source in the NSVS, 3 that match to a source in the ACVS, 7 that match to a source

⁷ The GCVS, NSV and NSVS were obtained from <http://www.sai.msu.su/groups/cluster/gcvs/gcvs/> on April 7 2009

⁸ Version 1.1 obtained from <http://www.astrouw.edu.pl/asas/?page=catalogues>

in the ROTSE catalog (3 of which are in the GCVS as well), and 23 that match to a Super-WASP source (2 of these are in their catalogue of previously identified variables). Two of the 29 candidate variables that match to a source in the GCVS (HAT-215-0001451 and HAT-215-0001491) actually match to the same source, V1097 Tau, a weak emission-line T Tauri star. Both stars are flagged as probable blends in our catalog, in this case HAT-215-0001491 is the correct variable while HAT-215-0001451 is the blend.

We inspect each of the 61 candidates with a potential match and find that the match is incorrect for 28 of them and correct for 33. For 17 of the 28 incorrect matches the candidate variable is flagged as a probable blend in our catalog. In 6 cases the candidate variable is flagged as a potential blend, in 3 cases it is flagged as an unlikely blend, and in 2 cases it is flagged as unblended. The match appears to be correct for three of the candidate variables flagged as probable blends. In addition to HAT-215-0001491, the stars HAT-239-0000221 and HAT-239-0000513 both match correctly to sources in the GCVS. These stars form a common proper motion, low mass binary system. Both stars are flagged as probable blends in our catalog. Each matches separately, and correctly, to a flare star in the GCVS (V0647 Her and V0639 Her respectively).

The 12 variables that match correctly to a source in the GCVS include 4 BY Draconis-type rotational variables, 6 UV Ceti-type flare stars, 1 INT class Orion variable of the T Tauri type, and 5 eclipsing systems. The EBs include the two W UMa-type contact systems DY CVn and V1104 Her, the two Algol-type systems DK CVn and V1001 Cas, and the M3V/white dwarf EB DE CVn (van den Besselaar et al. 2007).

Table 11, at the end of the paper, lists the first ten cross-identifications, the full table is available electronically with the rest of the catalog.

5.2. Match to ROSAT

We match all 2120 stars selected as potential variables to the ROSAT All-sky survey source catalog (Voges et al. 1999) using the US National Virtual Observatory catalog matching utilities. We use a 3.5σ positional matching criterion. A total of 237 of the variables match to an X-ray source, including 226 stars in our catalog of noneclipsing periodic variables, 14 of the EBs, and 24 of the 60 flare stars. A few of the variable stars are close neighbors where one is likely to be a blend of the other, so there are 232 distinct X-ray sources that are matched to. Table 12 at the end of the paper gives the cross-matches. The full table is available electronically with the rest of the catalog. In Section 6.2 we discuss the X-ray properties of the rotational variables.

6. DISCUSSION

6.1. Eclipsing Binaries

The 95 stars that we identify as potential EBs have periods ranging from $P = 0.193$ days to $P = 24.381$ days. We flag 17 of the candidate EBs as probable blends, 28 as potential blends, 21 as unlikely blends, and 29 as unblended. Figure 8 shows phased light curves for 12 of the EBs.

In addition to matching the candidate EBs to other variable star catalogs (§ 5.1) and to ROSAT (§ 5.2) we

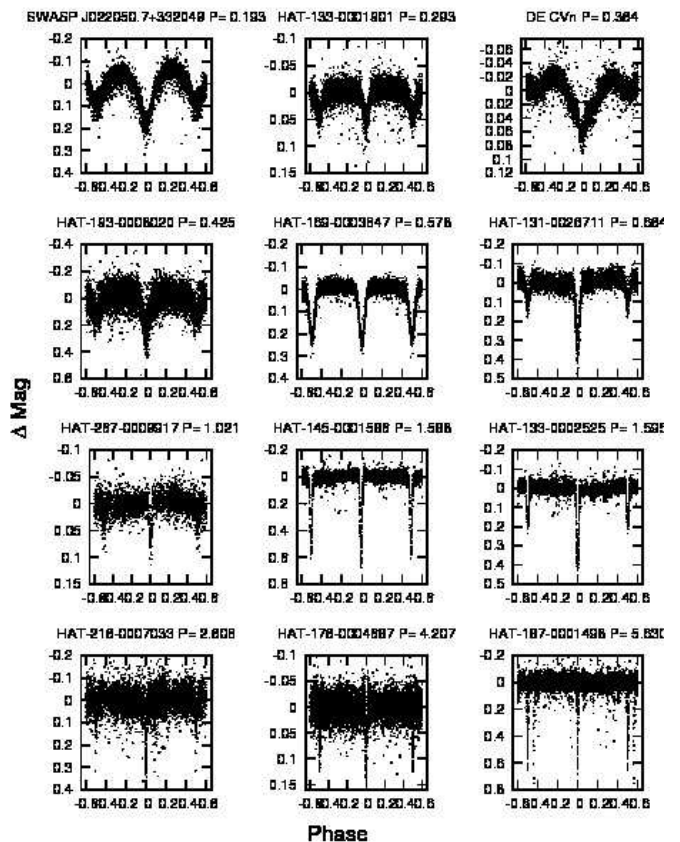


FIG. 8.— Example phased light curves for 12 of the 95 potential EBs found in the survey. The period listed is in days.

also checked for matches to previously studied objects using SIMBAD. The following objects had noteworthy matches:

1. *HAT-148-0000574*: matches to the X-ray source 1RXS J154727.5+450803, and was previously discovered to be an SB2 system by Mochnacki et al. (2002), we discuss this system in detail in § 6.1.1.
2. *HAT-216-0002918* and *HAT-216-0003316*: match to CCDM J04404+3127A and CCDM J04404+3127B, respectively, which form a common proper-motion $15''$ binary system. The two stars are both selected as candidate EBs with the same period, and are both flagged as potential blends in the catalog; based on a visual inspection of the light curves we conclude that the fainter component (*HAT-216-0003316*) is most likely the true $P = 2.048$ day EB. The fainter component, which has spectral type M3 on SIMBAD, also matches to the X-ray source RX J0440.3+3126.
3. *HAT-127-0008153*: matches to CCDM J03041+4203B, which is the fainter component in a common proper-motion $20''$ binary system. This star is flagged as a potential blend, the brighter component appears to match to the X-ray source 1RXS J030403.8+420319. Based on a visual inspection of the light curves we conclude that *HAT-127-0008153* is likely the true variable.
4. *HAT-169-0003847*: is $24''$ from the Super-WASP

variable 1SWASP J034433.95+395948.0, the two stars are blended in the HATNet images, however from a visual inspection of the light curves we conclude that HAT-169-0003847 is likely the true variable.

5. *HAT-192-0001841*: is $46''$ from a high proper-motion, K0 star BD+41 2679. The two stars may be members of a common proper-motion binary system (the former has a proper motion of 65.79 , -151.77 mas/yr in RA and DEC respectively, while the latter has 89.76 , -117.14 mas/yr).
6. *HAT-169-0003847*: is flagged as an unlikely blend, and we confirm that BD+41 2679 is not the true variable.
7. *HAT-193-0008020*: matches to GSC 03063-02208 and has a spectral type of M0e listed on SIMBAD (see also Mason et al. 2000).
8. *HAT-216-0007033*: matches to the X-ray source RX J0436.1+2733 and has spectral type M4 listed on SIMBAD.
9. *HAT-341-0019185*: is $43''$ from TYC 1097-291-1, the two stars appear to be members of a common proper motion binary system. HAT-341-0019185 is flagged as a probable blend in our catalog, though it does not appear that TYC 1097-291-1 is the real variable.

6.1.1. The Low-mass EB 1RXS J154727.5+450803

The EB HAT-148-0000574 matches to 1RXS J154727.5+450803. Using RV observations obtained with the Cassegrain spectrograph on the David Dunlap Observatory (DDO) 1.88 m telescope⁹, Mochnacki et al. (2002) found that this object is a $P = 3.54997 \pm 0.00005$ day double-lined spectroscopic binary system with component masses $\gtrsim 0.26 M_{\odot}$. This system, however, was not previously known to be eclipsing. Here we combine the published RV curves from Mochnacki et al. (2002) with the HATNet I-band light curve to provide preliminary estimates for the masses and radii of the component stars.

Figure 9 shows the EPD HATNet light curve phased at a period of $P = 3.550018$ days together with a model fit, while figure 10 shows a fit to the radial velocity observations taken from Mochnacki et al. (2002). Note the out of eclipse variations in the light curve, presumably due to spots on one or both of the components, which indicates that the rotation period of one or both of the stars is tidally locked to the orbital period. Since the HATNet light curve is not of high enough quality to measure the radii to better than a few percent precision, we do not fit a detailed spot model to the light curve, and instead fit a harmonic series to the out of eclipse observations and then subtract it from the full light curve. We model the light curve using the JKTEBOP program (Southworth, Maxted & Smalley 2004; Southworth et al. 2004) which is based on the Eclipsing Binary Orbit Program (EBOP; Popper & Etzel 1981;

TABLE 2
PARAMETERS FOR THE EB 1RXS J154727.5+450803

Coordinates and Photometry	
RA (J2000)	15:47:27.42 ^a
DEC (J2000)	+45:07:51.39 ^a
Proper Motions [mas/yr]	-259, 200 ^b
J	9.082 mag ^c
H	8.463 mag ^c
K	8.215 mag ^c
Ephemerides	
P	3.5500184 ± 0.0000018 day
HJD	$2451232.89534 \pm 0.00094$
Physical Parameters	
M_1	$0.2576 \pm 0.0085 M_{\odot}$
M_2	$0.2585 \pm 0.0080 M_{\odot}$
$R_1 = R_2$	$0.2895 \pm 0.0068 R_{\odot}$
RV Fit Parameters	
γ	-21.21 ± 0.41 km/s
K_1	55.98 ± 0.76 km/s
K_2	55.78 ± 0.83 km/s
e	0.0 ^d
LC Fit Parameters	
J_2/J_1	1.0734 ± 0.030
$(R_1 + R_2)/a$	0.0737 ± 0.0014
R_2/R_1	1.0 ^e
i	$86.673^{\circ} \pm 0.068^{\circ}$

^a SIMBAD

^b PPMX

^c 2MASS

^d fixed

^e fixed based on $q = 1.004 \pm 0.020$ from fitting the RV curves.

Etzel 1981; Nelson & Davis 1972), but includes more sophisticated minimization and error analysis routines. We used the DEBiL program (Devor 2005) to measure the eclipse minimum times from the light curve, which in turn were used with the RV curves to determine the ephemeris. In modeling the RV curves we fix $e = 0$ (Mochnacki et al. 2002, found $e = 0.008 \pm 0.007$; with the new ephemeris the 2σ upper limit on the eccentricity is $e < 0.04$), and we fix $k = R_2/R_1 = 1.0$ in modelling the light curve given $q = 1.00 \pm 0.02$ from the fit to the RV curves (the light curve is not precise enough to provide a meaningful constraint on k , however the constraint on $(R_1 + R_2)/a$ is robust). For completeness we note that we assumed quadratic limb darkening coefficients of $a = 0.257$, $b = 0.586$ for both stars (Claret 2000), which are appropriate for a $T_{\text{eff}} = 3000$ K, $\log g = 4.5$, solar metallicity star. The results are insensitive to the adopted limb darkening coefficients; we also performed the fit using the coefficients appropriate for a $T_{\text{eff}} = 4000$ K, $\log g = 4.5$ star and found negligible differences in the resulting parameters and uncertainties. The parameters for the system are given in table 2. Note that the 1σ errors given on the masses and radii are determined from a Monte Carlo simulation (Southworth et al. 2005). These are likely to be overly optimistic given the inaccurate treatment of the spots, and our assumption that the component radii are equal.

Table 3 lists the masses and radii of the 4 other known double-lined detached EBs with at least one main se-

⁹ Based on data obtained at the David Dunlap Observatory, University of Toronto

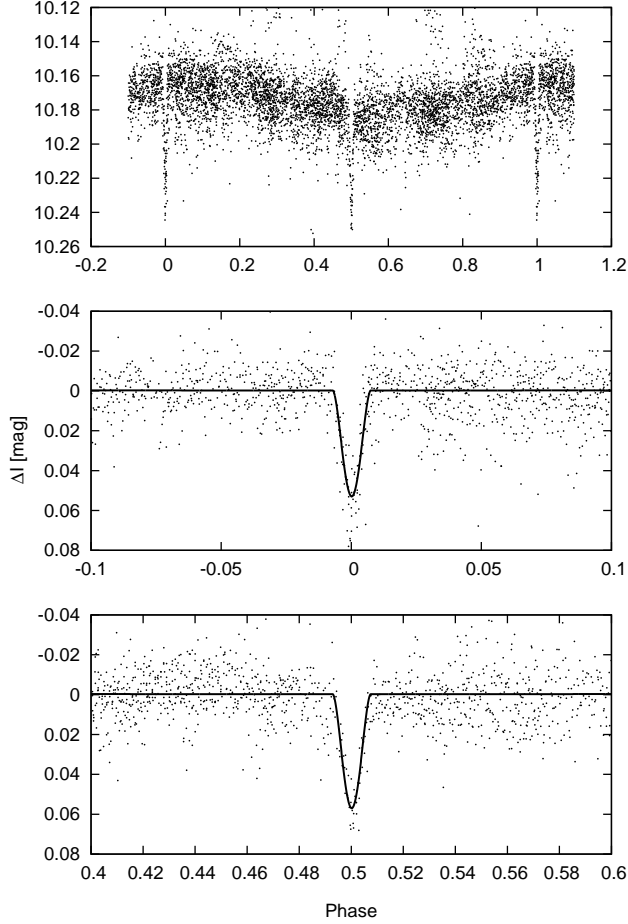


FIG. 9.— Phased HATNet I-band light curve for the low-mass EB 1RXS J154727.5+450803. The top panel shows the full EPD light curve, the bottom two panels show a model fit to the two eclipses after subtracting a harmonic series fit to the out of eclipse portion of the light curve.

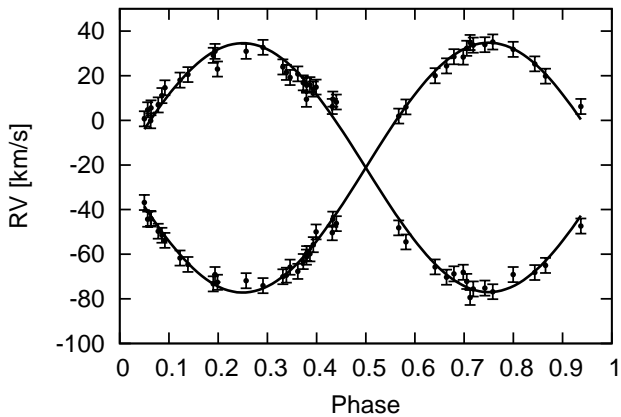


FIG. 10.— Circular orbit fit to the RV curves for the low-mass EB 1RXS J154727.5+450803. The observations are taken from Mochnacki et al. (2002).

sequence component that has a mass less than $0.3M_{\odot}$. We do not include RR Cae which is a white-dwarf/M-dwarf EB that has presumably undergone mass transfer (Maxted 2007). In figure 11 we plot the mass-radius relation for stars in the range $0.15M_{\odot} < M < 0.3M_{\odot}$.

Like the components of CM Dra and the secondary of GJ 3236, and unlike the components of SDSS-MEB-1 and the secondary of 2MASSJ04463285+190432, the components of 1RXS J154727.5+450803 have radii that are larger than predicted from the Baraffe et al. (1998) isochrones (if the age is $\gtrsim 200$ Myr). The radii are $\sim 10\%$ larger than the predicted radius in the 1.0 Gyr, solar metallicity isochrone. High precision photometric and spectroscopic follow-up observations, and a more sophisticated analysis of the data are need to confirm this.

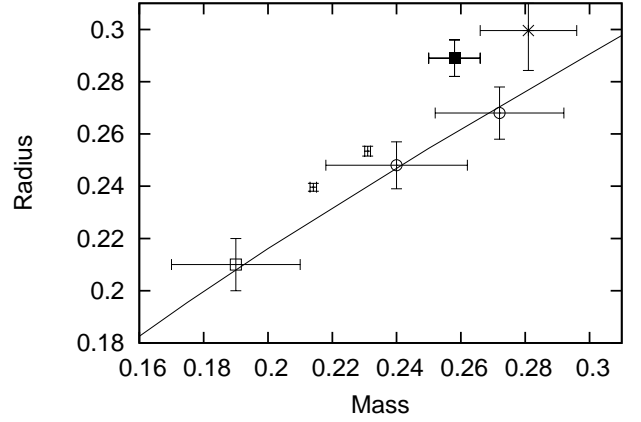


FIG. 11.— Mass-radius relation for 7 main sequence stars in double-lined DEBs with $M < 0.3M_{\odot}$. The two points with the smallest error bars are the components of CM Dra, the open circles are the components of SDSS-MEB-1, the open square is the secondary component of 2MASSJ04463285+190432, the X is the secondary component of GJ 3236, and the filled square marks the two components of 1RXS J154727.5+450803. The solid line shows the 1.0 Gyr, solar metallicity isochrone from Baraffe et al. (1998). Note that the error bars for 1RXS J154727.5+450803 do not incorporate systematic errors that may result from not properly modelling the spots or allowing the stars to have unequal radii.

6.2. Rotational Variables

Figure 12 shows example phased light curves for 12 randomly selected rotational variables found in our survey, while figure 13 shows the AoVHarm periodograms for five of these light curves. For the following analysis we only consider stars in our catalog of periodic noneclipsing variables that are identified as reliable detections for either the EPD or TFA light curves and that are not flagged as probable blends. If the variable is identified as a reliable detection for both the EPD and TFA light curves, we adopt the period found on the TFA light curve.

6.2.1. Variability Fraction-Color Relation

In figure 14 we compare the distribution of $V - K_S$ colors for periodic variables with peak-to-peak amplitudes greater than 0.01 mag to the distribution for all stars in the sample. We also show the fraction of stars that are variable at this level as a function of $V - K_S$. To estimate the fraction of stars in our sample that are blends we show the results separately for the full sample and for a sample restricted to stars that do not have a neighbor from the 2MASS catalog within $30''$ and are classified either as unblended or as unlikely blends. In figure 15 we compare the distribution of I_C magnitudes for periodic variables to the distribution for all stars in the sample.

TABLE 3
OTHER DOUBLE-LINED EBs WITH A VERY LATE M DWARF COMPONENT

Name	Period [days]	$M_1 [M_\odot]$	$M_2 [M_\odot]$	$R_1 [R_\odot]$	$R_2 [R_\odot]$
CM Dra	1.27	0.2310 ± 0.0009	0.2141 ± 0.0010	0.2534 ± 0.0019	0.2396 ± 0.0015
SDSS-MEB-1	0.407	0.272 ± 0.020	0.240 ± 0.022	0.268 ± 0.010	0.248 ± 0.009
2MASSJ04463285+190432	0.619	0.47 ± 0.05	0.19 ± 0.02	0.57 ± 0.02	0.21 ± 0.01
GJ 3236	0.771	0.376 ± 0.016	0.281 ± 0.015	0.3795 ± 0.0084	0.300 ± 0.015

REFERENCES. — CM Dra: Morales et al. (2009); Lacy (1977); Metcalfe et al. (1996); SDSS-MEB-1: Blake et al. (2008); 2MASSJ04463285+190432: Hebb et al. (2006); GJ 3236: the parameters listed for this system are determined by giving equal weight to the three models in Irwin et al. (2009b)

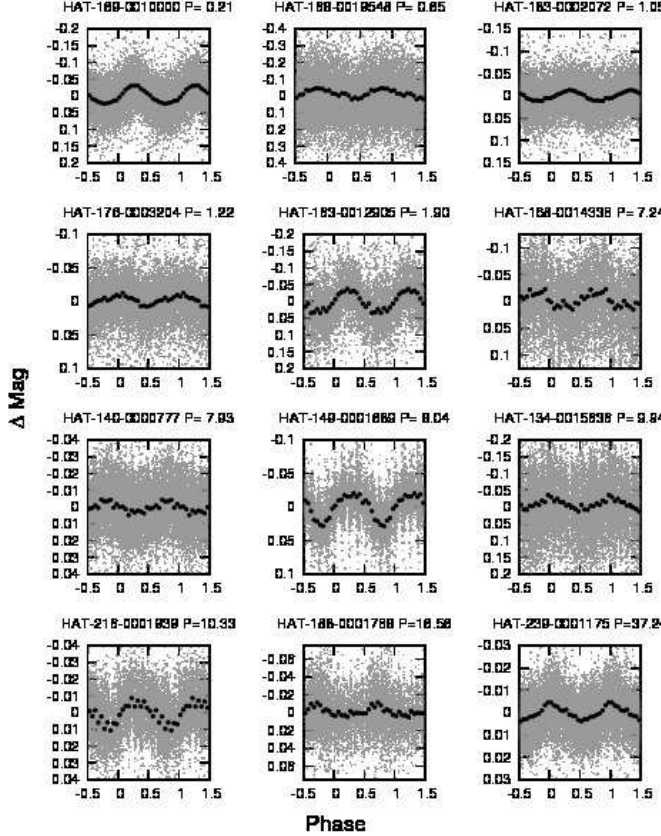


FIG. 12.— Phased EPD light curves for 12 randomly selected rotational variables found in the survey. The grey-scale points show all points in the light curve, the dark points show the binned light curve. The period listed is in days. The zero-point phase is arbitrary. For this figure we use the period found by applying AoVHarm to the TFA light curves.

The plotted relation for the fraction of stars that are variable as a function of color in figure 14 has been corrected for completeness by conducting sinusoid injection/recovery simulations to estimate our detection efficiency. In conducting these tests we divide the sample into 90 period/amplitude/color bins. We use color bins of $2.0 < V - K_S < 3.5$, $3.5 < V - K_S < 4.0$, $4.0 < V - K_S < 4.5$, $4.5 < V - K_S < 5.0$ and $5.0 < V - K_S < 6.0$, three period bins of 0.1-1 day, 1-10 days, and 10-100 days, and 5 amplitude bins logarithmically spanning 0.01 to 1.0 mag. We have also considered using magnitude bins rather than color bins for determining the completeness correction, and have found that the resulting differences in the relation shown in figure 14 are negligible. The resolution of the grid was

set by the available computational resources. For each bin we randomly select 1000 stars with the appropriate color (for color bins with fewer than 1000 stars we select with replacement). For each selected star we then choose a random period and amplitude drawn from uniform-log distributions over the bin and inject a sine curve with that period/amplitude and a random phase into the light curve of the star. If both EPD and TFA light curves are available for the star we inject the same signal into both light curves. We do not reduce the amplitude for the injection into the TFA light curve, this may cause us to slightly overestimate our detection efficiency for periods longer than ~ 10 days. If the star was identified as a variable or a potential variable by our survey, we first remove the true variable signal from the light curve by fitting a harmonic series to the phased light curve before injecting the simulated signal. We then process the simulated signals through the AoVHarm algorithm using the same selection parameters as used for selecting the real variables. We do not apply by-eye selections on the simulated light curves; we estimate below the systemic uncertainty that results from this.

To get the completeness corrected variability fraction we weight each real detected variable by $1/f$ where f is the fraction of simulated signals that are recovered for the period/amplitude/color bin that the real variable falls in. We find that we are roughly $\sim 70\%$ complete over our sample of stars for peak-to-peak amplitudes greater than 0.01 mag and periods between 0.1 and 100 days. For $\sim 97\%$ of the recovered simulations the recovered frequency is within 0.001 day^{-1} of the injected frequency. The recovery rate is relatively insensitive to the period and color and depends most significantly on the amplitude. For amplitudes between 0.01 mag and 0.022 mag the recovery rate is $\sim 65\%$, whereas for amplitudes above 0.05 mag the recovery rate is $\sim 85\%$. Above 0.05 mag the recovery rate is independent of amplitude.

To estimate the systematic uncertainty due to not applying the by-eye selection, we note that only $\sim 1\%$ of stars with $P < 10$ days that passed the automatic selections for AoVHarm were classified by eye as unreliable detections. For stars with $P > 10$ days, we classified $\sim 30\%$ of the stars passing the automatic selections as unreliable detections. Assuming that 1% of the automatically selected simulations with $P < 10$ days would be rejected by eye, and that 30% of the automatically selected simulations with $P > 10$ days would be rejected by eye, we put a lower limit of $\sim 60\%$ on the completeness of our sample. We conclude, therefore, that the true completeness of our sample for variable stars with peak-to-peak amplitudes greater than 0.01 mag is between 60 – 70%.

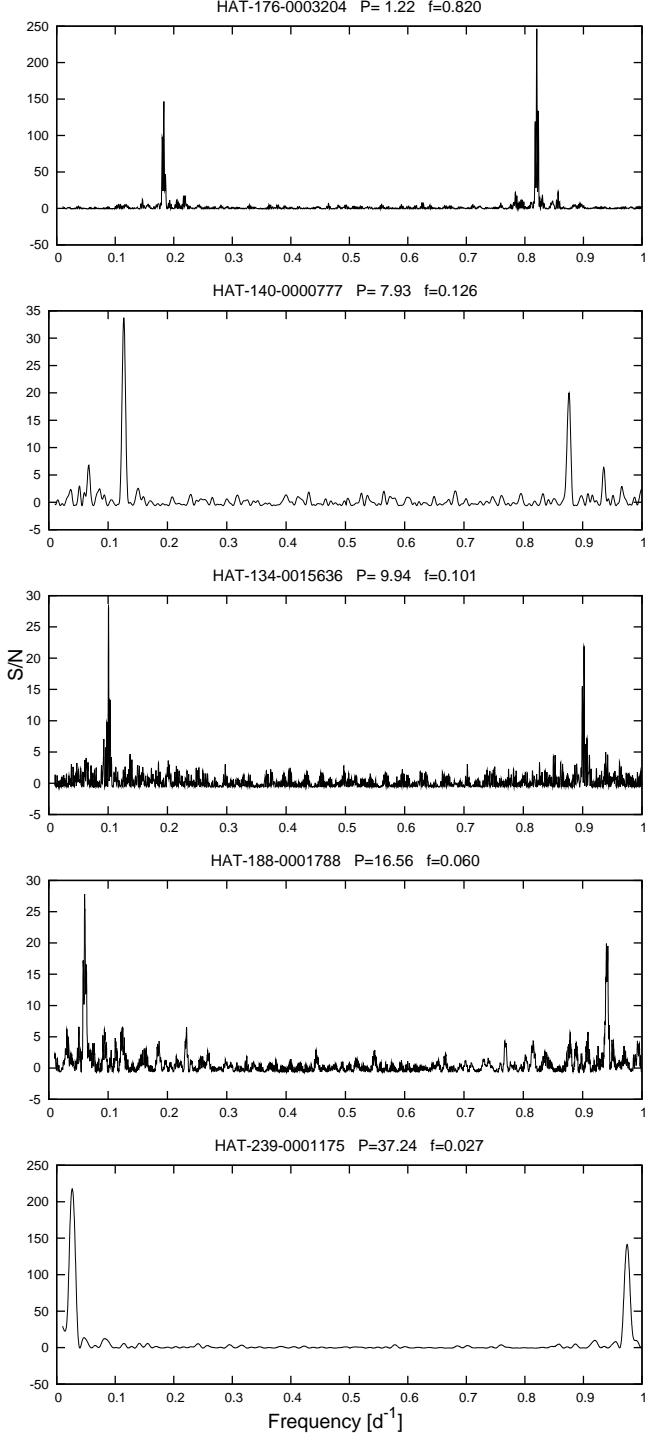


FIG. 13.— AoVHarm periodograms for 5 of the example light curves shown in fig. 12. The periodograms have been normalized to have zero median and unit standard deviation after iterative 5σ clipping. The peak period/frequency for each periodogram is listed in units of days and cycles per day respectively. The secondary peak in each case is the sidereal day alias of the primary peak. In each case we assume that the highest S/N peak corresponds to the correct period. While it is possible, though unlikely, that the secondary peak may actually be the true period and not the alias, there is no way in general to determine this; some ambiguity is inevitable.

As seen in figure 14 the fraction of stars that are de-

tected as variables increases steeply with decreasing stellar mass for the sample where blending is not likely to be significant. While $\lesssim 2\%$ of stars in this sample with $M \gtrsim 0.7 M_{\odot}$ are found to be variable with peak-to-peak amplitude > 0.01 mag, approximately half of the stars with $M \lesssim 0.2 M_{\odot}$ are detected as variables at this level. We find that an exponential relation of the form

$$\text{Var. Frac.} = (0.0016^{+0.0011}_{-0.00066})e^{(0.929 \pm 0.13)(V-K_S)} \quad (14)$$

fits the observed relation over the color range $2.0 < V - K_S < 6.0$. Note that if the completeness correction is not applied, the leading coefficient is reduced to $0.001^{+0.00069}_{-0.00041}$, but the coefficient in the exponential is 0.969 ± 0.14 which is consistent with the coefficient in eq. 14 to within the uncertainties. We conclude therefore that there does not appear to be a significant color bias in our selection of variables and that the color dependence given in eq. 14 is correct. Including a by-eye rejection rate of 30% for light curves with $P > 10$ days increases the leading coefficient by 0.00021 and does not change the coefficient in the exponent. We therefore conclude that the statistical uncertainties given in eq. 14 are significantly larger than the systematic uncertainties in the relation.

For the larger sample of stars the variable fraction-color relation follows eq. 14 with a constant value of 0.0162 ± 0.0021 added in. In other words, for a random star in our sample, there is a $\sim 1.6\%$ chance that the star will be blended with a nearby variable, show variations in its light curve with an amplitude > 0.01 mag, and that the star will not be flagged as a probable blend by our blending classification scheme. We estimate that 26% of the variable stars in the larger sample are blends; most of these are the bluer stars for which the real variability fraction is comparable to or less than 1.6%.

6.2.2. Period-Amplitude Relation

For FGK stars there is a well-known anti-correlation between stellar activity measured from emission in the H and K line cores, or from H α emission, and the Rossby number (R_O , the ratio of the rotation period to the characteristic time scale of convection, see Noyes et al. 1984), which saturates for short periods. Similar anti-correlations with saturation have been seen between R_O and the X-ray to bolometric luminosity ratio (e.g. Pizzolato et al. 2003), and between R_O and the amplitude of photometric variability (e.g. Messina et al. 2001; Hartman et al. 2009). Main sequence stars with $M \lesssim 0.35 M_{\odot}$ are fully convective (Chabrier & Baraffe 1997), so one might expect that the rotation-activity relation breaks down, or significantly changes, at this mass. Despite this expectation, several studies have indicated that the rotation-activity relation (measured using $v \sin i$ and H α respectively) may continue even for late M-dwarfs (Delfosse et al. 1998; Mohanty & Basri 2003; Reiners & Basri 2007). Recently, however, West & Basri (2009) have found that rotation and activity may not always be linked for these stars.

In figure 16 we plot the rotation period against the peak-to-peak amplitude for stars in several color bins. The peak-to-peak amplitude is calculated for the EPD light curves as described in section 4; for stars observed in multiple fields we take the amplitude of the combined

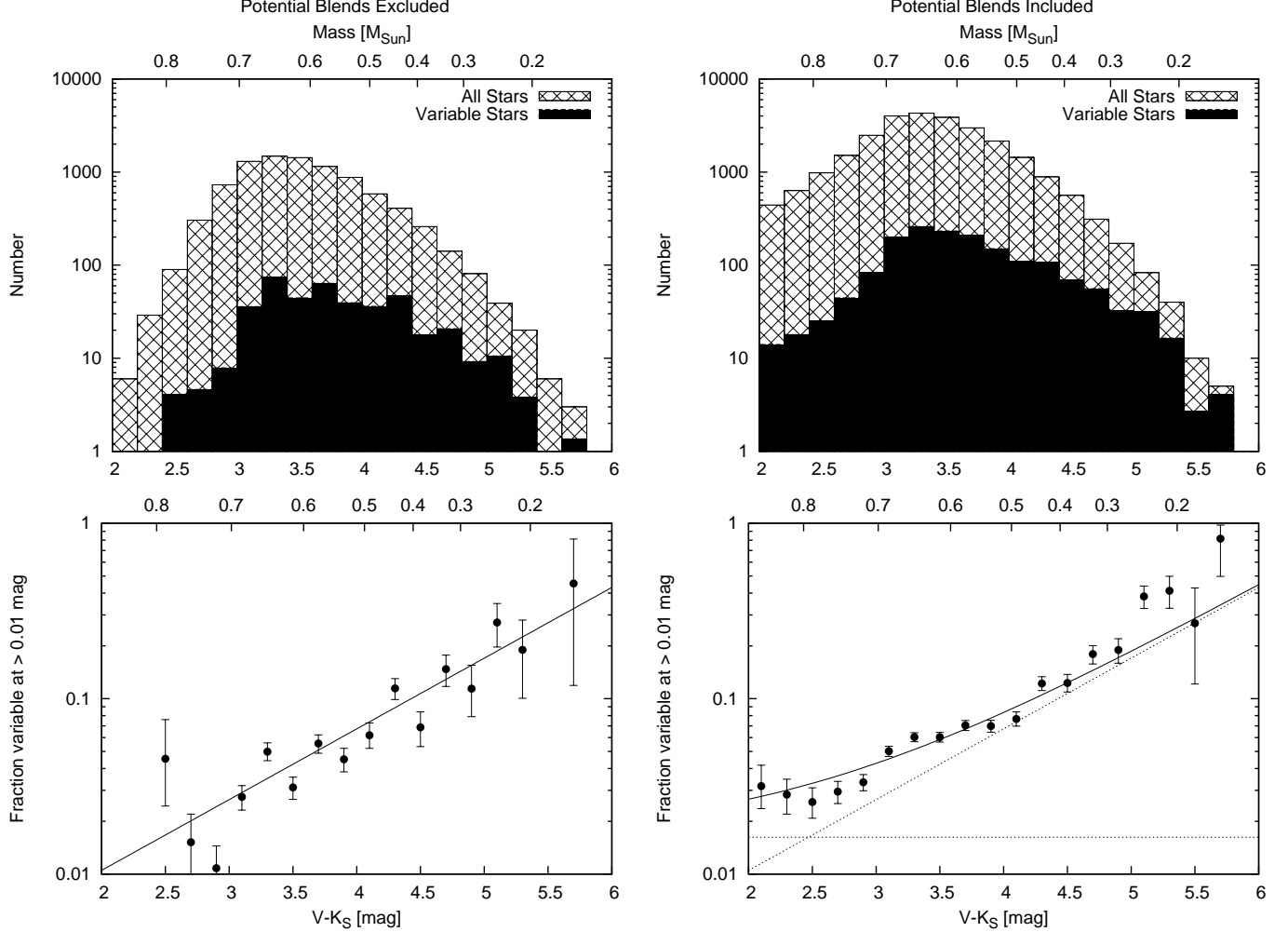


FIG. 14.— Top: The distribution of $V - K_S$ colors for variable stars compared to the distribution of $V - K_S$ for both variable and non-variable stars in the sample. On the right we show all 26884 stars with $V - K_S > 2$ and the 1190 noneclipsing periodic variables with $V - K_S > 2$ that have a peak-to-peak amplitude greater than 0.01 mag, are flagged as being secure detections, and are not flagged as probable blends. On the left we limit the sample to the 8944 stars and 298 variables that, in addition to the previous restrictions, also do not have any neighbors in the 2MASS catalog within $30''$ and are not flagged as potential blends. On the top axis we show the corresponding main sequence stellar masses determined by combining the empirical $V - K_S$ vs. M_K main-sequence for stars in the Solar neighborhood given by Johnson & Apps (2009) with the mass- M_K relation from the Baraffe et al. (1998) 4.5 Gyr, solar-metallicity isochrone with $L_{\text{mix}} = 1.0$. We used the relations from Carpenter (2001) to convert the CIT K magnitudes from the isochrones into the 2MASS system. The distribution for variable stars is biased toward redder $V - K_S$ colors relative to the distribution for all stars. The decrease in the total number of stars in the sample red-ward of $V - K_S \sim 3.5$ is due to the V -band magnitude limit of the PPMX survey. Bottom: The completeness corrected fraction of stars that are variable with peak-to-peak R or I_C amplitude > 0.01 mag as a function of $V - K_S$; we use the same samples of stars on the left and right as for the top panels. On the left panel the fraction increases exponentially with color (solid line (left), sloped dotted line (right), eq. 14) such that $\lesssim 2\%$ of stars with $M \gtrsim 0.7 M_\odot$ are variable with peak-to-peak amplitudes > 0.01 mag while approximately 50% of stars with $M \lesssim 0.2 M_\odot$ are variable at this level. On the right panel we also include a constant frequency of 0.0162 ± 0.0021 (constant dotted line) that is independent of color, and corresponds to the blend frequency. The solid line at right shows the sum of the constant term and the exponential term. We estimate that 26% of the potential variables included in the upper right panel are blends with real variable stars.

light curve. Stars without an available EPD light curve are not included in the plot. A total of 1279 stars are included in the plot. We mark separately the 301 variables that are not flagged as potential blends and do not have a 2MASS neighbor within $30''$. For stars with $V - K_S < 5.0$ (corresponding roughly to $M \gtrsim 0.25 M_\odot$) the photometric amplitude and the period are anti-correlated at high significance. There appears to be a cut-off period, such that the period and amplitude are uncorrelated for stars with periods shorter than the cut-off, and are anti-correlated for stars with periods longer than the cut-off. Hartman et al. (2009) find a saturation threshold of $R_O = 0.31$, which for a $0.6 M_\odot$ star corresponds to a

period of ~ 8 days (assuming $(B - V)_0 = 1.32$ for stars of this mass, and using the empirical relation between the convective time scale and $(B - V)_0$ from Noyes et al. 1984). This is consistent with what we find for the bluest stars in our sample. For stars with $V - K_S > 5.0$ ($M \lesssim 0.25 M_\odot$), the period and amplitude are not significantly correlated, at least for periods $\lesssim 30$ days. This result suggests that the distribution of starspots on late M dwarfs is uncorrelated with rotation period over a large period range, and is perhaps at odds with $H\alpha/v \sin i$ studies which indicate a drop in activity for very late M-dwarf stars with $v \sin i \lesssim 10$ km/s (e.g. Mohanty & Basri 2003).

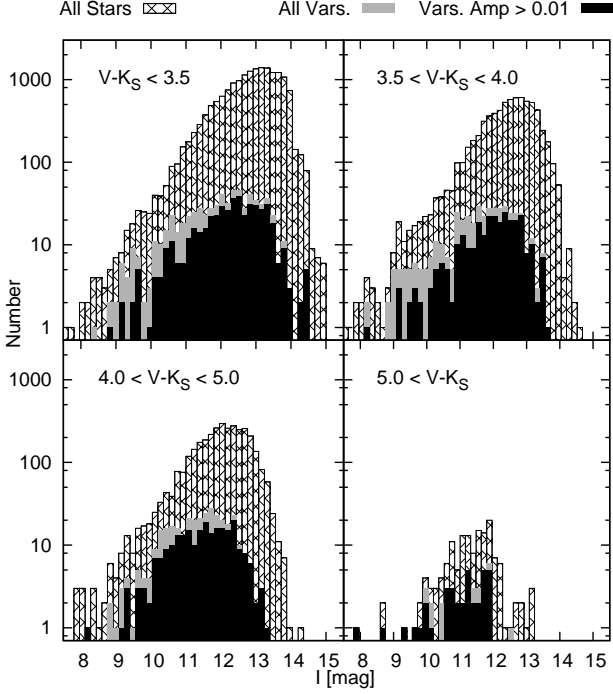


FIG. 15.— The distribution of I_C magnitudes for all stars, all periodic variable stars, and all periodic variable stars with peak-to-peak amplitudes greater than 0.01 mag is shown for different $V - K_S$ bins.

6.2.3. Period-Color/Period-Mass Relation

In figure 17 we show the relation between period and color. For stars with $V - K_S \lesssim 4.5$ the measured distribution of $\log P$ is peaked at ~ 20 days with a broad tail toward shorter periods and a more rapid drop-off for longer periods. Note that the cut-off for longer periods may be due to the correlation between period and amplitude for these stars; stars with periods longer than ~ 20 days may be harder to detect and not intrinsically rare. The peak of the distribution appears to be correlated with color such that redder stars are found more commonly at longer periods than bluer stars. For stars with $V - K_S \gtrsim 4.5$ the distribution changes significantly such that the $\log P$ distribution appears to be more or less flat between ~ 0.3 and ~ 10 days, while red stars with $P \gtrsim 10$ days are uncommon.

In Figure 18 we compare the mass-period distribution for stars in our survey to the results from other surveys of field stars and open clusters. We choose to use mass for the comparison rather than observed colors because a consistent set of colors is not available for all surveys. The masses for stars in our survey are estimated from their $V - K_S$ colors (see Fig. 14).

We take data from the Mount Wilson, Vienna-KPNO (Strassmeier et al. 2000), and ASAS (Kiraga & Stępień 2007) samples of field stars with rotation periods. For the Mount Wilson sample we use the compilation by Barnes (2007), the original data comes from Baliunas et al. (1996) and from Noyes et al. (1984). For the Vienna-KPNO sample we only consider stars which are listed as luminosity class V. We estimate the masses for stars in the Mount Wilson and Vienna-KPNO samples using the same $V - K_S$ to mass conversion that we use for our own

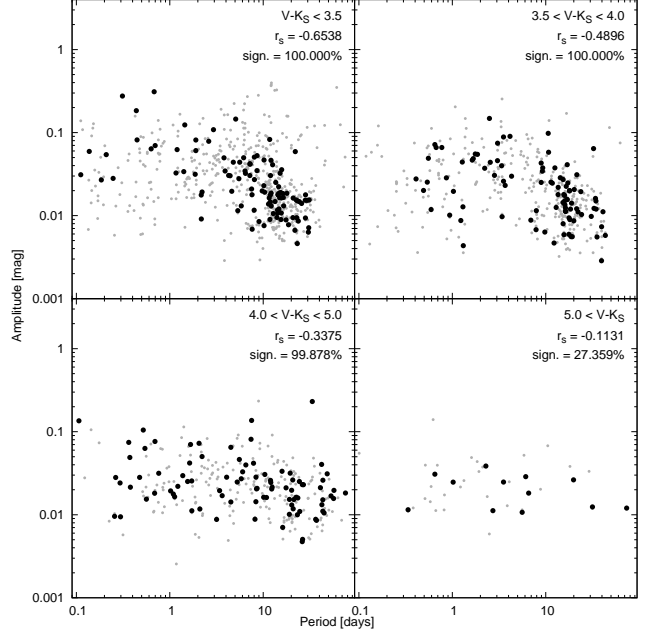


FIG. 16.— Rotation period vs. peak-to-peak photometric amplitude for 1279 stars. Dark filled circles show variables that do not have a 2MASS neighbor within $30''$ and are flagged as unblended or as unlikely blends, while the grey-scale filled circles show all other variables that are not flagged as probable blends. We divide the sample into 4 bins by $V - K_S$ color, corresponding roughly to $M \gtrsim 0.6M_\odot$, $0.5M_\odot \lesssim M \lesssim 0.6M_\odot$, $0.25M_\odot \lesssim M \lesssim 0.5M_\odot$, and $M \lesssim 0.25M_\odot$, from blue to red. We also list the Spearman rank-order correlation coefficient and the statistical significance of the correlation for each sample (note that negative values of r_s imply that the period and amplitude are anti-correlated). The statistics are given for the stars shown with the dark filled points. For stars with $V - K_S < 5.0$ the period and peak-to-peak amplitude are anti-correlated at high significance (for stars with $4.0 < V - K_S < 5.0$ the significance is higher than $1 - 10^{-5}$ when the grey-scale points are included in the calculation). The relation appears to be saturated for periods $\lesssim 5$ days, with the saturation period increasing for decreasing stellar mass. For stars with $V - K_S > 5.0$ ($M \lesssim 0.25M_\odot$), the period and amplitude are not significantly correlated for $P \lesssim 30$ days.

sample. The V and K_S magnitudes for these field stars are taken from SIMBAD where available. For the ASAS sample we use the masses determined from the absolute M_V magnitudes of the stars by Kiraga & Stępień (2007).

We also compare our sample to four open clusters with ages between 100 – 200 Myr and to three open clusters with ages of ~ 600 Myr. These include: M35 (~ 180 Myr; Meibom et al. 2009), three clusters observed by the MONITOR project, including M50 (~ 130 Myr; Irwin et al. 2009a), NGC 2516 (~ 150 Myr; Irwin et al. 2007), and M34 (~ 200 Myr; Irwin et al. 2006), M37 (~ 550 Myr; Hartman et al. 2009), Coma Berenices (~ 600 Myr; Collier Cameron et al. 2009), and the Hyades (~ 625 Myr; Radick et al. 1987, 1995; Prosser et al. 1995). For the MONITOR clusters we use the mass estimates given in their papers, these are based on the I_C -mass relation from the appropriate Baraffe et al. (1998) isochrone for the age/metallicity of each cluster. For M35, M37 and the Hyades we use the mass estimates derived from the V, I_C -mass relations from the appropriate YREC (An et al. 2007) isochrones for each cluster. For Coma Berenices we use the mass- M_K relation discussed in Fig. 14 and assume a distance of 89.9 pc for

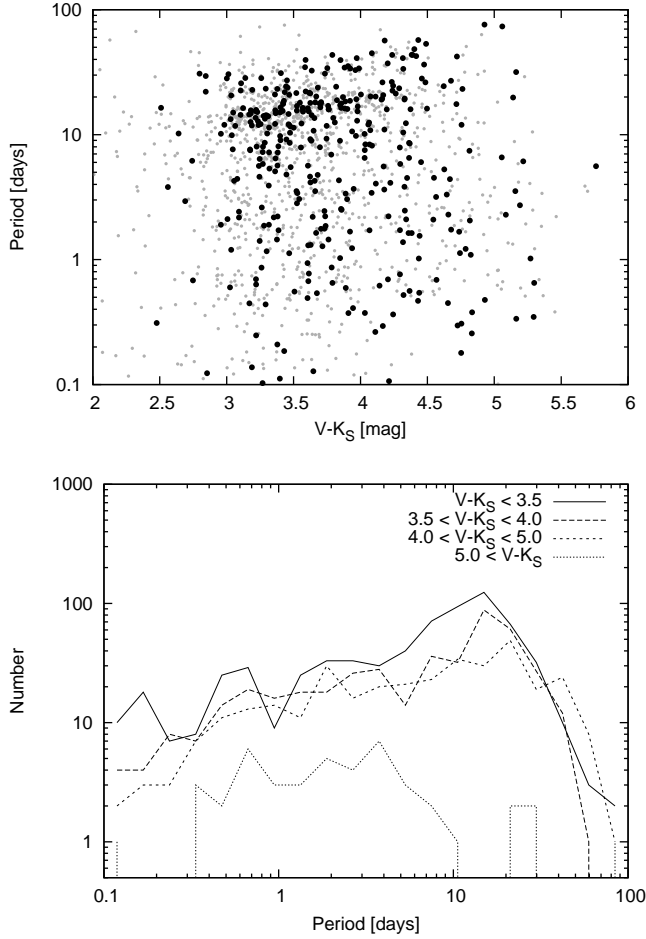


FIG. 17.— Top: Period vs. $V - K_S$ for stars in our catalog of periodic variables that are flagged as being secure detections for at least one detection method, are not flagged as having incorrect period determinations for that method, and are not flagged as probable blends. There appears to be a paucity of stars with $P > 10$ days and $V - K_S > 4.5$ or $V - K_S < 3$. Bottom: The distributions of periods are shown for four color bins. For the three bluest color bins there appears to be a correlation between period and color, such that the mode period is longer for redder stars. For stars with $V - K_S \gtrsim 4.5$, on the other hand, the period distribution appears to be biased to shorter periods. Using a K-S test, we find that the probability that the stars in any two of the different color bins are drawn from the same distribution is less than 0.01% for all combinations except the for the combination of the two intermediate color bins. For that combination the probability is $\sim 12\%$.

all stars (van Leeuwen 1999). For M35 we only include 214 stars from the Meibom et al. (2009) catalog that lie near the main sequence in V , B and I_C , and we exclude any stars which have a proper motion membership probability less than 80%, or an RV membership probability less than 80% as determined by Meibom et al. (2009). We expect that the stars in our sample, and in the other field star samples, have a range of ages, but on average will be older than the stars in the open clusters.

The sample of stars with rotation periods presented here is substantially richer than is available for other surveys of field stars. This is especially the case for later spectral types. The Mt. Wilson and Vienna-KPNO surveys primarily targeted G and early K stars, so there is not much overlap in stellar mass between those samples and our sample. The ASAS survey, on the other

hand, covers a similar mass range as our survey, but for a much smaller sample of stars (periods were found for 31 out of 180 X-ray active stars). The few Mt. Wilson stars with estimated masses $\lesssim 0.8 M_\odot$ do show an anti-correlation between mass and period, and have periods that are longer than the majority of stars in our sample. The Vienna-KPNO stars, on the other hand, have periods that cluster around ~ 10 days, which is closer to the mode of the period distribution for stars of comparable mass in our sample. Since the Vienna-KPNO stars were selected as showing spectroscopic evidence for chromospheric activity before their periods were measured photometrically, this sample is presumably biased to shorter period active stars compared to the Mt. Wilson sample. Given the correlation between photometric amplitude and rotation period, we would also expect our sample to be biased toward shorter period stars relative to the Mt. Wilson sample. The ASAS stars with $M \gtrsim 0.5 M_\odot$ generally have shorter periods than the stars in our survey; this is most likely due to the restriction of the ASAS survey to X-ray active stars.

When compared to the open cluster samples we see clear evidence for evolution in the rotation periods of low-mass stars. Stars in the younger clusters have shorter periods at a given mass, on average, than stars in our sample. The discrepancy becomes more apparent for stars with $M \lesssim 0.5 M_\odot$ for which the period and mass appear to be positively correlated in the young cluster samples while they are anti-correlated in our sample. Looking at the ~ 600 Myr clusters, again the periods of stars in our sample are longer at a given mass, on average, than the periods of the cluster stars, however in this case the mode of the period distribution for the cluster stars appears to be closer to the mode of the period distribution for our sample than it is for the younger clusters. The lowest mass stars in the older clusters also do not show as significant a correlation between mass and period as do the lowest mass stars in the younger clusters. For stars with $M \lesssim 0.3 M_\odot$ the available field star and older open cluster samples are too sparse to draw any conclusions from when comparing to our sample. For the younger clusters, we note that the distribution of periods for the lowest mass stars is even more strongly peaked toward short periods than it is in our sample. This suggests that these stars do lose angular momentum over time, despite not having a tachocline. A more detailed comparison of these data to models of stellar angular momentum evolution is beyond the scope of this paper.

6.2.4. Period-X-ray Relation

Figure 19 shows the fraction of variables that match to an X-ray source as a function of period. This fraction is constant at $\sim 22\%$ for periods less than ~ 4 days, for longer periods the fraction that matches to an X-ray source decreases as $\sim P^{-0.7}$. Following Agüeros et al. (2009) we calculate the ratio of X-ray to J-band flux via

$$\log_{10}(f_X/f_J) = \log_{10} f_X + 0.4J + 6.30 \quad (15)$$

where 1 count s^{-1} in the 0.1-2.4 keV energy range is assumed to correspond on average to $f_X = 10^{-11} \text{ erg cm}^{-2} \text{ s}^{-1}$. In figure 20 we plot the flux ratio as a function of rotation period for samples of variables separated by their $V - K_S$ color. The X-ray flux is anti-correlated

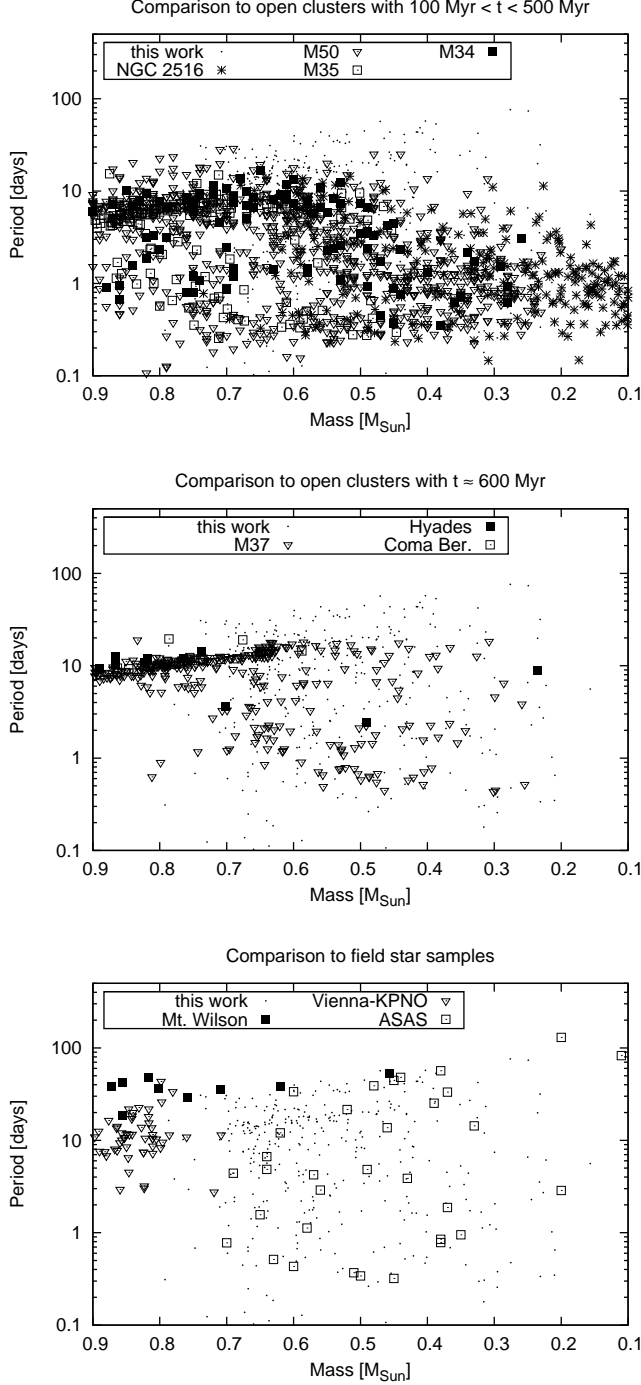


FIG. 18.— A comparison of the mass-period distribution for stars in our survey to the results from other surveys. We only include stars from our survey that do not have a 2MASS neighbor within $30''$ and are classified either as an unlikely blend or as unblended. See the text for a description of the other data sources. For clarity we make the comparison separately for field stars, open clusters with $100 \text{ Myr} < t < 500 \text{ Myr}$ and for three open clusters with $t \sim 600 \text{ Myr}$. The rotation periods of stars in our sample at a given mass appear to be longer, on average, than the periods of stars in the open clusters; this is true across all mass ranges covered by our survey. The rotation periods from the Vienna-KPNO survey appear to be comparable, at a given mass, to the periods of stars in our sample, while the periods from the Mt. Wilson survey appear to be generally longer than the periods from our survey. It is likely that our survey, the Vienna-KPNO survey and the ASAS survey are biased toward high-activity, shorter period stars than the Mt. Wilson survey is.

with the rotation period for stars with $M \gtrsim 0.25 M_{\odot}$, for stars with $M \lesssim 0.25 M_{\odot}$ there is still a hint of an anti-correlation, though it is of low statistical significance (the false alarm probability is $\sim 20\%$). This result is similar to what we found for the photometric amplitude-period relation.

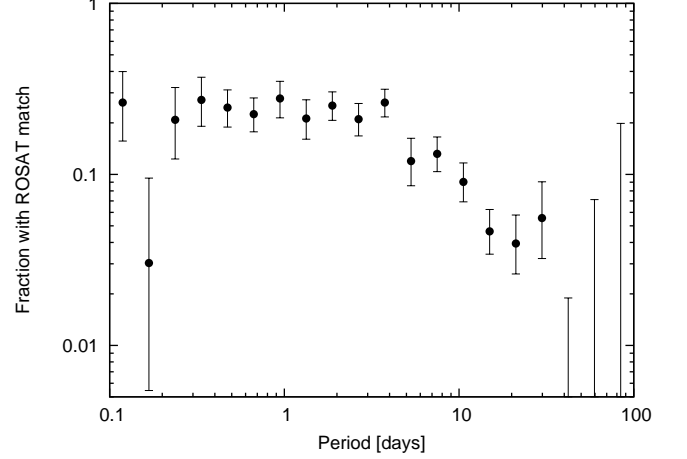


FIG. 19.— The fraction of non-EB periodic variable stars that match to a ROSAT source as a function of rotation period. The errorbars for the 3 longest period bins show 1σ upper-limits. For stars with rotation periods less than ~ 4 days the fraction that matches to an X-ray source is constant at $\sim 22\%$, for longer periods the fraction decreases as $\sim P^{-0.7}$.

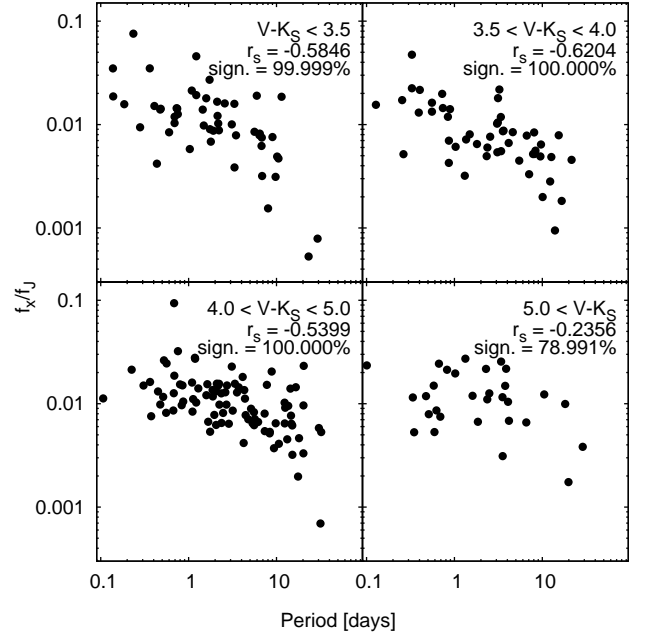


FIG. 20.— The ratio of 0.1-2.4 keV X-ray flux to J -band near infrared flux vs. the rotation period for non-EB periodic variable stars that match to a ROSAT source. We divide the sample into the same 4 color bins used in fig. 16. We also list the Spearman rank-order correlation coefficient and the statistical significance of the correlation for each sample. The X-ray flux is anti-correlated with the rotation period at high significance for stars with $V - K_S < 5.0$. For stars with $V - K_S > 5.0$ ($M \lesssim 0.25 M_{\odot}$) there is still a hint of an anti-correlation, though it is of low statistical significance.

6.3. Flares

In figure 21 we compare the distribution of periods for stars with detected large-amplitude long-duration flares to the distribution for stars without such flare detections. A total of 32 of the 60 flare stars have a robust period determination and are not flagged as a probable blend. The period detection frequency of $\sim 50\%$ for flare stars is significantly higher than that for all other stars ($\lesssim 5\%$). This result is expected if stellar flaring is associated with the large starspots that give rise to continuous photometric variations. As seen in figure 21, the distribution of periods for flare stars is concentrated toward shorter periods than the distribution for non-flare stars. The longest period found for a flare star is 18.2 days whereas 31% of the non-flare stars with period determinations have periods greater than 18.2 days. Conducting a K-S test we find that the probability that the two samples are drawn from the same distribution is less than 10^{-4} .

Figure 22 compares the distribution of $V - K_S$ for the flare stars to the distribution for the full sample. From this figure it is clear that flare detections are more common for redder stars.

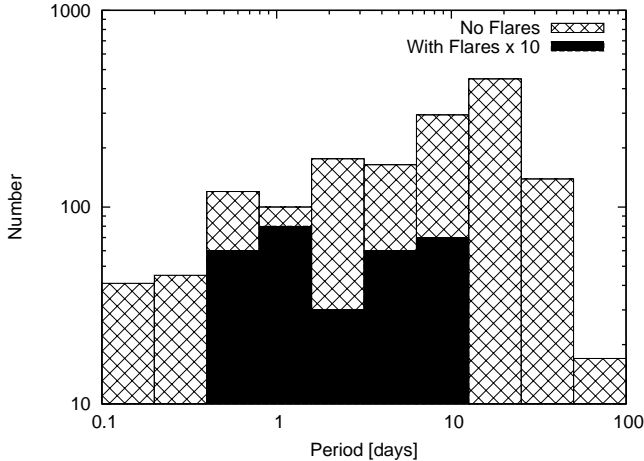


FIG. 21.— Comparison between the period distributions for stars with detected large-amplitude long-duration flares, and stars without such a flare detected. Note the absence of long-period stars with flares. For clarity we have multiplied the flare star period distribution by a factor of 10.

6.4. Multi-periodic Variables

In Section 3.4 we described a search for multiperiodic variability that was applied to a subset of the K/M dwarf light curves. A number of the stars appear to vary with multiple periods. We highlight here two of the more significant cases, HAT-094-0007885 and HAT-123-0003441. These two stars have $V - K_S = 3.8$ and $V - K_S = 3.9$ respectively, which correspond to stellar masses of $M \sim 0.5 M_\odot$. Figure 23 shows the DFT power spectra for each of these variables after successive prewhitening cycles. HAT-094-0007885 has two significant frequencies: $f_0 = 4.5240512 \text{ d}^{-1}$ and $f_1 = 0.2318221 \text{ d}^{-1}$. The amplitude and/or frequency of both components change during the total time span of 162 days. This varying phase/amplitude leads to remnant power near the peak frequencies (or at their aliases).

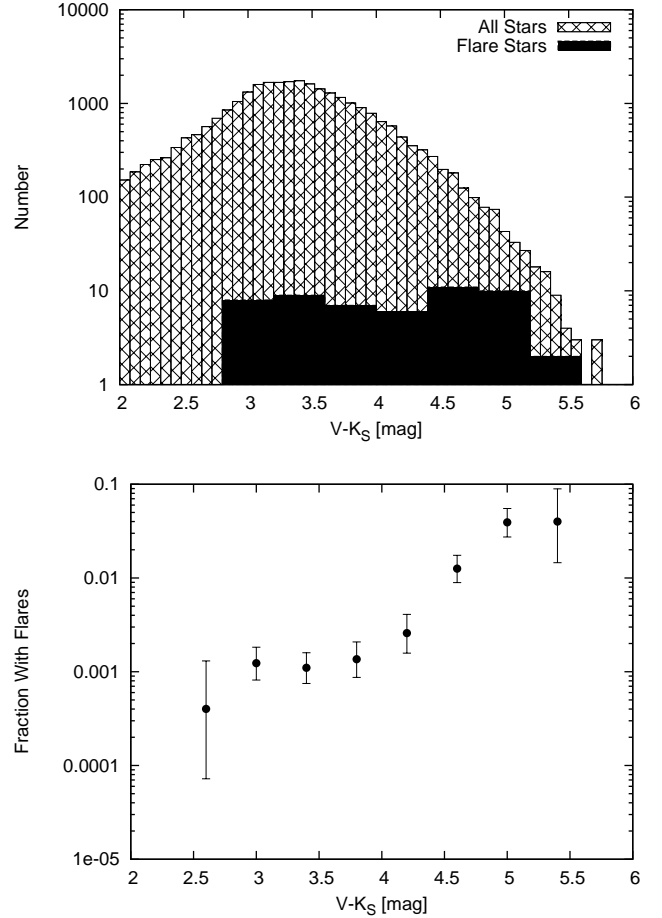


FIG. 22.— Top: The distribution of $V - K_S$ colors for the 60 stars with high amplitude flares detected compared to the distribution of $V - K_S$ colors for all 27,560 stars in the sample. The distribution for flare stars is biased toward redder $V - K_S$ colors relative to the distribution for all stars. Note that we use a 5 times higher binning resolution for the full sample. Bottom: The fraction of stars with a high amplitude flare detection is plotted against $V - K_S$. For stars with $V - K_S < 4.0$ less than $\sim 0.1\%$ of stars had a flare detected, for stars with $V - K_S > 4.5$ the fraction is $\gtrsim 1\%$.

Note that $(f_0 - 1)/2 + f_1 = 1.99215 \text{ d}^{-1}$, so it is possible that f_1 is an alias the primary signal f_0 . The nearest 2MASS source to this star is more than $30''$ away, and all sources within $1'$ are $\gtrsim 2.5$ mag fainter. This star has a blending flag of 0, indicating that the variation is most likely not due to blending with a neighbor. HAT-123-0003441 has two significant frequencies: $f_0 = 2.80539 \text{ d}^{-1}$ and $f_1 = 2.33122 \text{ d}^{-1}$. Note that when the frequency search is applied to the light curves without applying TFA, the two identified frequencies are $f_0 = 1.80367 \text{ d}^{-1}$ and $f_1 = 1.32918 \text{ d}^{-1}$, which are the 1 d^{-1} aliases of the TFA frequencies. The frequency corresponding to the period identified with the AoVHarm algorithm applied to the TFA light curve for this star is $f = 1.80415 \text{ d}^{-1}$. This star has 6 faint neighbors within $60''$, we assign a blending flag of 1 to this star, indicating that at least the f_0 component signal is unlikely to be due to blending with a nearby variable.

It is unclear what the physical origin of multiple frequencies would be for either of these stars if they are single $M \sim 0.5 M_\odot$ dwarfs. If the variations are not due to nearby stars that are unresolved in the HATNet im-

ages and are aligned by chance with the low-mass stars, it may be that these are multiple star systems with the components rotating at different periods.

7. CONCLUSION

In this paper we have presented the results of a variability survey conducted with HATNet of field K and M dwarfs selected by color and proper motion. We used a variety of variability selection techniques to identify periodic and quasi-periodic variables, and have also conducted a search for large amplitude, long-duration flare events. Out of a total sample of 27,560 stars we selected 2120 that show potential variability, including 95 that show eclipses in their light curves, and 60 that show flares. We inspected all automatically selected light curves by eye, and flagged 1806 stars (including those with flares) as being secure variability detections. Because the HATNet images have poor spatial resolution, variability blending is a significant problem. We therefore implemented an automated routine to classify selected non-flare variables as probable blends, potential blends, unlikely blends, or as unblended. Altogether we found 1568 variables that are classified as secure detections and are not classified as probable blends. We estimate, however, that 26% of these stars may still be blends with fainter variables. The 1568 variables includes 78 stars that show eclipses in their light curves. We identified 64 flare events in 60 stars, 35 of these stars are also selected as potential periodic or quasi-periodic variables (all 35 are considered reliable detections, and 32 are not flagged as probable blends). We matched the sample of potential variables to other catalogs, and found that 61 lie within $2'$ of a previously identified variable, while 2059 do not. Including only flare stars and variables that are classified as secure detections and are not classified as probable blends, 38 (including 5 EBs) lie within $2'$ of a previously identified variable, so that 1530 are new identifications.

One of the eclipsing binaries that we identified is the previously known SB2 system 1RXS J154727.5+450803. By combining the published RV curves for the component stars with the HATNet I band light curve, we obtained initial estimates for the masses and radii of the component stars (Tab. 2). The system is one of only a handful of known double-lined eclipsing binaries with component masses less than $0.3 M_{\odot}$. While we caution that the errors on the component radii are likely to be underestimated due to systematic errors that have not been considered in this preliminary analysis, it is interesting that the radii do appear to be larger than predicted if the system is older than ~ 200 Myr. With a magnitude $V \sim 13.4$, this system is only slightly fainter than the well-studied binary CM Dra ($V \sim 12.90$) which has been the anchor of the empirical mass-radius relation for very late M dwarfs. 1RXS J154727.5+450803 is thus a promising target for more detailed follow-up to obtain high precision measurements of the fundamental parameters of the component stars. With additional follow-up, the large sample of 78 probable late-type eclipsing binaries presented in this paper should prove fruitful for further investigations of the fundamental parameters of low-mass stars.

The majority of the variable stars that we have identified are likely to be BY Dra type variables, with the

measured period corresponding to the rotation period of the star. This is the largest sample of rotation periods presented to date for late-type field stars. We discussed a number of broad trends seen in the data, including an anti-correlation between the rotation period and the photometric amplitude of variability, an exponential relation between $V - K_S$ color and the fraction of stars that are variable, a positive correlation between period and the $V - K_S$ color for stars with $V - K_S \lesssim 4.5$, a relative absence of stars with $P \gtrsim 10.0$ days and $V - K_S \gtrsim 4.5$, and an anti-correlation between the rotation period and the ratio of X-ray to J band flux. The correlations between period and activity indicators including the amplitude of photometric variability and the X-ray emission are consistent with the well-known rotation-age-activity-mass relations for F, G, and K dwarfs. The data presented here may help in further refining these relations. Our data hints at a change in the rotation-activity connection for the least massive stars in the sample ($M \lesssim 0.25 M_{\odot}$). The anti-correlation between period and amplitude appears to break down for these stars, and similarly the period-X-ray anti-correlation is less significant for these stars than for more massive stars. This is potentially at odds with previous studies which used H α to trace activity and $v \sin i$ to infer rotation period, and found that the period-activity anti-correlation extends to very late-type M dwarfs. Comparing our sample to other field and open cluster samples, we find that the rotation periods of stars in our sample are generally longer than the periods found in open clusters with $t \lesssim 620$ Myr, which implies that K and M dwarf stars continue to lose angular momentum past the age of the Hyades. This appears to be true as well for stars with $M \lesssim 0.25 M_{\odot}$, though these stars generally have shorter periods than more massive stars in our sample.

We have also conducted a search for flare events in our light curves, identifying 64 events in 60 stars. Due to the difficulty of distinguishing between a flare and bad photometry in an automated way, there are likely to be many flare events in the light curves that we do not identify. We therefore do not attempt to draw conclusions about the total occurrence rate of flaring (for a recent determination of this frequency using data from the Sloan Digital Sky Survey, see Kowalski et al. 2009). We find that the distribution of $V - K_S$ colors for flare stars is biased toward red colors, implying that the flare frequency increases with decreasing stellar mass, which has been known for a long time (Ambartsumyan et al. 1970, see also Kowalski et al. 2009). We find that roughly half the flare stars are detected as periodic variables, which is a significantly higher fraction than for the full sample of stars. This is in line with the expectation that stellar flaring is associated with the presence of significant starspots, and is consistent with the finding by Kowalski et al. (2009) that the flaring frequency of active M dwarfs showing H α emission is ~ 30 times higher than the flaring frequency of inactive M dwarfs. We also find that the distribution of periods for flare stars is biased toward shorter periods, again as expected from the rotation-activity connection.

Finally we identified several potentially multi-periodic variables from a search conducted on a subset of the light curves, and we highlighted two examples. We speculate that the variation in these cases is either due to blending

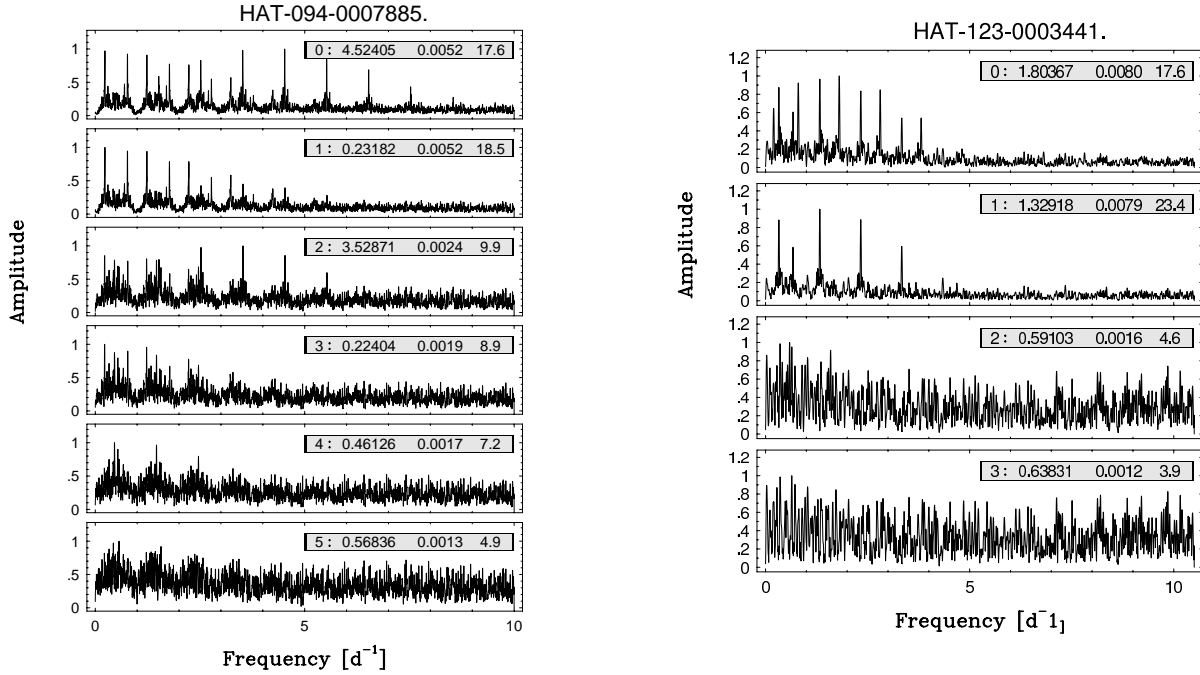


FIG. 23.— DFT power spectra for two multi-periodic variables. The power spectra are displayed from top to bottom after successively prewhitening the light curve against identified frequencies. The numbers in each panel give the prewhitening cycle, the peak frequency in d^{-1} , the amplitude of the peak in mag, and the S/N of the peak. For HAT-123-0003441 we show the DFT power spectra for the light curve without TFA applied.

with nearby variable stars, or else these may be multi-star systems where each detected period corresponds to the rotation period of a different component star. As far as we are aware, there is no known pulsation mechanism in K and M dwarf stars that would give rise to millimagnitude level photometric variations with different periods.

We would like to thank Lev Or-Tal for calculating the upper limit to the eccentricity for the eclipsing binary 1RXS J154727.5+450803. HATNet operations have been funded by NASA grants NNG04GN74G, NNX08AF23G and SAO IR&D grants. G.Á.B. acknowledges support from the Postdoctoral Fellowship of the NSF Astronomy and Astrophysics Program (AST-0702843). G.K. thanks

the Hungarian Scientific Research Foundation (OTKA) for support through grant K-81373. T.M. acknowledges support from the ISRAEL SCIENCE FOUNDATION (grant No. 655/07). The Digitized Sky Surveys were produced at the Space Telescope Science Institute under U.S. Government grant NAG W-2166. The images of these surveys are based on photographic data obtained using the Oschin Schmidt Telescope on Palomar Mountain and the UK Schmidt Telescope. The plates were processed into the present compressed digital form with the permission of these institutions. This research has made use of data obtained from or software provided by the US National Virtual Observatory, which is sponsored by the National Science Foundation. This research has made use of the SIMBAD database, operated at CDS, Strasbourg, France.

REFERENCES

- Abazajian, K. N., et al. 2009, *ApJS*, 182, 543
 Agüeros, M. A., et al. 2009, *ApJS*, 181, 444
 Akerlof, C., et al. 2000, *AJ*, 119, 1901
 An, D., Terndrup, D. M., Pinsonneault, M. H., Paulson, D. B., Hanson, R. B., & Stauffer, J. R. 2007, *ApJ*, 655, 233
 Ambartsumyan, V. A., Mirzoyan, L. V., Parsamyan, E. S., Chavushyan, O. S., & Erastova, L. K. 1970, *Astrofizika*, 6, 7
 Bakos, G., Noyes, R. W., Kovács, G., Stanek, K. Z., Sasselov, D. D., & Domsa, I. 2004, *PASP*, 116, 266
 Bakos, G., Noyes, R. W., Latham, D. W., Csák, B., Gálfi, G., & Pál, A. 2006, in “Tenth Anniversary of 51 Peg-b: Status of and prospects for hot Jupiter studies” eds. L. Arnold, F. Bouchy & C. Moutou (Frontier Group: Paris), p.184-186
 Bakos, G. Á., et al. 2009, *ApJ*, in press, arXiv:0901.0282
 Baliunas, S. L., et al. 1995, *ApJ*, 438, 269
 Baliunas, S., Sokoloff, D., & Soon, W. 1996, *ApJ*, 457, L99
 Baraffe, I., Chabrier, G., Allard, F., & Hauschildt, P. H. 1998, *A&A*, 337, 403
 Barnes, S. A. 2007, *ApJ*, 669, 1167
 Beatty, T. G., et al. 2007, *ApJ*, 663, 573
 Bessell, M. S., & Brett, J. M. 1988, *PASP*, 100, 1134
 Blake, C. H., Torres, G., Bloom, J. S., & Gaudi, B. S. 2008, *ApJ*, 684, 635
 Bonatto, Ch., Bica, E., & Girardi, L. 2004, *A&A*, 415, 571
 Carpenter, J. M. 2001, *AJ*, 121, 2851
 Chabrier, G., & Baraffe, I. 1997, *A&A*, 327, 1039
 Chabrier, G., Baraffe, I., Allard, F., & Hauschildt, P. 2000, *ApJ*, 542, 464
 Chabrier, G., Gallardo, J., & Baraffe, I. 2007, *A&A*, 472, L17
 Claret, A. 2000, *A&A*, 363, 1081

- Collier Cameron, A., et al. 2009, MNRAS, in press, arXiv:0908.0189
- Cousins, A. W. J. 1976, MmRAS, 81, 25
- Delfosse, X., Forveille, T., Perrier, C., & Mayor, M. 1998, A&A, 331, 581
- Demory, B.-O., et al. 2009, A&A, in press, arXiv:0906.0602v1
- Devor, J. 2005, ApJ, 628, 411
- Duncan, D. K., et al. 1991, ApJS, 76, 383
- Edelson, R. A., & Krolik, J. H. 1988, ApJ, 333, 646
- Elias, J. H., Frogel, J. A., Hyland, A. R., & Jones, T. J. 1983, AJ, 88, 1027
- Elias, J. H., Frogel, J. A., Matthews, K., & Neugubauer, G. 1982, AJ, 87, 1029
- Etzel, P. B. 1981, NATO ASI, p. 111
- Fernandez, J., et al. 2009, ApJin press, arXiv:0906.2207
- Gould, A., & Morgan, C. W. 2003, ApJ, 585, 1056
- Guinan, E. F., & Engle, S. G. 2009, arXiv:0901.1860
- Hartman, J. D., Bakos, G., Stanek, K. Z., & Noyes, R. W. 2004, AJ, 128, 1761
- Hartman, J. D., Gaudi, B. S., Holman, M. J., McLeod, B. A., Stanek, K. Z., Barranco, J. A., Pinsonneault, M. H., & Kalirai, J. S. 2008, ApJ, 675, 1254
- Hartman, J. D., et al. 2009, ApJ, 691, 342
- Hebb, L., Wyse, R. F. G., Gilmore, G., & Holtzman, J. 2006, AJ, 131, 555
- Høg, E., et al. 2000, A&A, 355, L27
- Irwin, J., Aigrain, S., Hodgkin, S., Irwin, M., Bouvier, J., Clarke, C., Hebb, L., & Moraux, E. 2006, MNRAS, 370, 954
- Irwin, J., Hodgkin, S., Aigrain, S., Hebb, L., Bouvier, J., Clarke, C., Moraux, E., & Bramich, D. M. 2007, MNRAS, 377, 741
- Irwin, J., Aigrain, S., Bouvier, J., Hebb, L., Hodgkin, S., Irwin, M., & Moraux, E. 2009a, MNRAS, 392, 1456
- Irwin, J., et al. 2009b, ApJin press, arXiv:0906.4365
- Johnson, J. A., & Apps, K. 2009, ApJin press, arXiv:0904.3092
- Kasting, J. F., Whitmire, D. P., & Reynolds, R. T. 1993, Icarus, 101, 108
- Kazarovets, E. V., Samus, N. N., & Durlevich, O. V. 1998, IBVS, 4655
- Kharchenko, N. V. 2001, Kinematika i Fizika Nebesnykh Tel, 17, 409
- Kholopov, P. N.(ed) 1982, The New Catalogue of Suspected Variable Stars, Moscow:Nauka
- Kiraga, M., & Stepień, K. 2007, AcA, 57, 149
- Kovács, G., Zucker, S., & Mazeh, T. 2002, A&A, 391, 369
- Kovács, G., Bakos, G., & Noyes, R. W. 2005, MNRAS, 356, 557
- Kowalski, A. F., Hawley, S. L., Hilton, E. J., Becker, A. C., West, A. A., Bochanski, J. J., & Sesar, B. 2009, arXiv:0906.2030
- Krautter, J. 1996, in Light Curves of Variable Stars: a Pictorial Atlas, eds. C. Sterken and C. Jaschek (Cambridge: Cambridge University Press), 53
- Lacy, C. H. 1977, ApJ, 218, 444
- Landolt, A. U. 1992, AJ, 104, 340
- Lammer, H., et al. 2007, Astrobiology, 7, 185
- Lomb, N. R. 1976, A&SS, 39, 447
- López-Morales, M. 2005, ApJ, 631, L1120
- López-Morales, M. 2007, ApJ, 660, L732
- Lupton, R. 1993, Statistics in Theory and Practice, (Princeton: Princeton University Press)
- Luyten, W. J. 1922, Lick Observatory Bulletin, 10, 135
- Mamajek, E. E., & Hillenbrand, L. A. 2008, ApJ, 687, 1264
- Marigo, P., Girardi, L., Bressan, A., Groenewegen, M. A. T., Silva, L., & Granato, G. L. 2008, A&A, 482, 883
- Marquardt, D. W. 1963, Journal of the Society for Industrial and Applied Mathematics, 11, 431
- Mason, K. O., et al. 2000, MNRAS, 311, 456
- Maxted, P. F. L., O'Donoghue, D., Morales-Rueda, L., Napiwotzki, R., & Smalley, B. 2007, MNRAS, 376, 919
- Meibom, S., Mathieu, R. D., & Stassun, K. G. 2009, ApJ, 695, 679
- Messina, S., Rodonò, M., & Guinan, E. F. 2001, A&A, 366, 215
- Metcalfe, T. S., Mathieu, R. D., Latham, D. W., & Torres, G. 1996, ApJ, 456, 356
- Mirzoyan, L. V., Ambaryan, V. V., Garibdzhanyan, A. T., & Mirzoyan, A. L. 1989, Astrophysics, 31, 567
- Mochmacki, S. W., et al. 2002, AJ, 124, 2868
- Mohanty, S., & Basri, G. 2003, ApJ, 583, 451
- Monet, D. G., et al. 2003, AJ, 125, 984
- Morales, J. C., et al. 2009, ApJ, 691, 1400
- Nataf, D. M., Stanek, K. Z., & Bakos, G. A. 2009, AcA submitted, arXiv:0904.4696
- Nelson, B., & Davis, W. D. 1972, ApJ, 174, 617
- Norton, A. J., et al. 2007, A&A, 467, 785
- Noyes, R. W., Hartmann, L., Baliunas, S. L., Duncan, D. K., & Vaughn, A. H. 1984, ApJ, 279, 763
- Pál, A., & Bakos, G. Á. 2006, PASP, 118, 1474
- Pál, A. 2009, Ph.D. Thesis, Eötvös Loránd University, arXiv:0906.3486
- Perryman, M. A. C., et al. 1997, A&A, 323, L49
- Pizzolato, N., Maggio, A., Micela, G., Sciortino, S., & Ventura, P. 2003, A&A, 397, 147
- Pojmanski, G. 2002, AcA, 52, 397
- Popper, D. M., & Etzel, P. B. 1981, AJ, 86, 102
- Prosser, C. F., et al. 1995, PASP, 107, 211
- Radick, R. R., Thompson, D. T., Lockwood, G. W., Duncan, D. K., & Baggett, W. E. 1987, ApJ, 321, 459
- Radick, R. R., Lockwood, G. W., Skiff, B. A., & Thompson, D. T. 1995, ApJ, 452, 332
- Reiners, A., & Basri, G. 2007, ApJ, 656, 1121
- Reyle, C., & Robin, A. C. 2004, A&A, 421, 643
- Ribas, I. 2003, A&A, 398, 239
- Ribas, I. 2006, Ap&SS, 304, 89
- Röser, S., Schilbach, E., Schwan, H., Kharchenko, N. V., Piskunov, A. E., & Scholz, R.-D. 2008, A&A, 488, 401
- Samus, N. N., Durlevich, O. V., Zharova, A. V., Kazarovets, E. V., Kireeva, N. N., Pastukhova, E. N., Williams, D. B., & Hazen, M. L. 2006, Astronomy Letters, 32, 263
- Scargle, J. D. 1982, ApJ, 263, 835
- Schwarzenberg-Czerny, A. 1989, MNRAS, 241, 153
- Schwarzenberg-Czerny, A. 1996, ApJ, 460, L107
- Shporer, A., Mazeh, T., Moran, A., Bakos, G., & Kovács, G. 2007, in "Transiting Extrasolar Planets Workshop, ASP Conference Series 366" eds. C. Afonso, D. Welde, & Th. Henning, 99
- Shporer, A., Bakos, G. Á., Mazeh, T., Kovács, G., & Sipőcz, B. 2009, IAU Symposium, 253, 331
- Skrutskie, M. F., et al. 2006, AJ, 131, 1163
- Skumanich, A. 1972, ApJ, 171, 565
- Southworth, J., Maxted, P. F. L., & Smalley, B. 2004, MNRAS, 351, 1277
- Southworth, J., Zucker, S., Maxted, P. F. L., & Smalley, B. 2004, MNRAS, 355, 986
- Southworth, J., Smalley, B., Maxted, P. F. L., Claret, A., & Etzel, P. B. 2005, MNRAS, 363, 529
- Stellingwerf, R. F. 1978, ApJ, 224, 953
- Strassmeier, K., Washuettl, A., Granzer, T., Scheck, M., & Weber, M. 2000, A&AS, 142, 275
- Szulágyi, J., Kovács, G., & Welch, D. L. 2009, A&A, 500, 917
- Torres, G., & Ribas, I. 2002, ApJ, 567, 1140
- Torres, G., Lacy, C. H., Marschall, L. A., Sheets, H. A., & Mader, J. A. 2006, ApJ, 640, 1018
- Torres, G. 2007, ApJ, 671, L65
- van den Besselaar, E. J. M., et al. 2007, A&A, 466, 1031
- van Leeuwen, F. 1999, A&A, 341, L71
- Voges, W., et al. 1999, A&A, 349, 389
- West, A. A., & Basri, G. 2009, ApJ, 693, 1283
- Wilson, O. C., & Bappu, M. K. V. 1957, ApJ, 125, 661
- Wilson, O. C. 1978, ApJ, 226, 379
- Yong, D., & Lambert, D. L. 2003, PASP, 115, 796

APPENDIX

A. CATALOG OF VARIABLE STARS

We present the data as 3 separate catalogs of candidate variable stars, including: continuous periodic variables selected with the AoVHarm technique and not flagged as an EB during the visual inspection of either the EPD or TFA

light curves, eclipsing binaries, and flare events. All three catalogs will be made available in electronic form from the CDS archive server¹⁰ as well as from the HATNet website¹¹. Light curves for the variable stars will be made available through the Harvard University Time Series Center¹² and through NStED¹³. There are a total of 2033 stars that are in the first catalog, 95 candidate EB stars in the second, and 64 flare events from 60 stars in the third. Note that some of the EBs and flare stars are included in the primary catalog as well. Altogether 2120 stars are included in at least one of the catalogs.

In the primary catalog of periodic variables we include the internal HAT-ID of each source, its J2000 position from 2MASS, the periods, S/N, peak-to-peak amplitudes and quality flags for the AoVHarm algorithm applied to the TFA and EPD light curves, and the blending flag described in § 4. For convenience we also include the PPMX proper motion, the 2MASS photometry, the estimated V magnitude for each source, and the number of 2MASS neighbors within $30''$ of each source. For both periods we list the peak-to-peak amplitude in the I_C and/or R bands, determined for both the EPD and TFA light curves phased at that period. See § 4 for a description of how the amplitude is measured. Note that the TFA light curves used for the amplitude determination have not been processed with signal-reconstruction mode TFA, as a result these amplitudes are generally lower than the real amplitude of the star, and are lower than the amplitudes measured on the EPD light curves. Tables 4-6 at the end of the paper show the first ten entries in this catalog. For display purposes we split the catalog into 3 separate tables, in the full electronic version of the catalog the tables are joined.

In the catalog of candidate eclipsing binary stars we include the HAT-ID, position, proper motion, 2MASS photometry, and V magnitude, together with the period, period uncertainty, epochs of primary and secondary eclipse (if the secondary is detected) and their respective uncertainties, the durations of the primary and secondary eclipses, the number of 2MASS neighbors within $30''$ of the source, and the blending flag. Tables 7-8 at the end of the paper show the first ten entries in this catalog.

In the catalog of flare events we include the HAT-ID, position, proper motion, 2MASS photometry, and V magnitude, together with the time of the flare peak, the peak intensity relative to the non-flaring intensity (A in Eq. 9), and the decay time of the flare (τ in Eq. 9). Tables 9-10 at the end of the paper show the first ten entries in this catalog.

¹⁰ <http://cdsarc.u-strasbg.fr>

¹¹ <http://hatnet.hu/>

¹² <http://timemachine.iic.harvard.edu/>

¹³ <http://nsted.ipac.caltech.edu>

TABLE 4
CATALOG OF CANDIDATE PERIODIC VARIABLE STARS. I: ASTROMETRIC AND PHOTOMETRIC DATA

ID	RA ^a h:m:s	DE ^a deg:m:s	pmRA ^b mas/yr	pmDE ^b mas/yr	Jmag ^c mag	Hmag ^c mag	Kmag ^c mag	Vmag mag	Vref ^d	Nnbr ^e	Bl1 ^f	Bl2 ^f
HAT-086-0001701	00:13:38.42	+52:45:05.0	35.13	-36.72	9.519	8.763	8.658	12.136	1	2	1	9
HAT-086-0004017	23:54:23.85	+54:41:26.9	35.30	35.51	9.565	8.804	8.643	12.235	1	2	2	9
HAT-086-0005153	23:51:18.20	+54:35:16.2	76.13	-7.77	9.906	9.239	9.060	12.822	1	4	2	9
HAT-086-0005542	00:16:56.01	+50:37:49.0	146.68	-27.87	9.980	9.349	9.137	12.767	1	3	2	9
HAT-086-0005602	00:16:01.61	+48:55:56.9	-83.81	51.47	10.008	9.409	9.186	12.870	1	0	3	9
HAT-086-0006520	23:56:16.37	+52:42:34.8	19.41	-45.99	10.260	9.590	9.478	12.227	1	6	2	9
HAT-086-0008187	23:45:32.05	+55:40:58.0	-41.95	-6.38	10.462	9.840	9.657	12.791	1	6	2	9
HAT-086-0009482	00:04:57.67	+49:58:49.1	93.81	2.31	10.594	9.933	9.757	13.413	1	0	1	9
HAT-086-0011792	23:46:30.54	+54:48:56.1	23.13	-21.70	10.861	10.228	10.042	13.191	1	4	2	9
HAT-086-0013793	23:43:29.95	+51:50:15.8	40.15	14.37	11.126	10.514	10.366	13.280	1	3	2	9
...												

^a J2000, from 2MASS

^b from PPMX

^c from 2MASS

^d Source for Vmag (0: PPMX (Tycho-2), 1: Transformed from USNO-B1.0, 2: Transformed from 2MASS)

^e Number of other 2MASS sources within 30''

^f Blending Flag, Bl1 is determined from 2MASS, Bl2 is determined from SDSS. (0: unblended, 1: unlikely blend, 2: possible blend, 3: probable blend, 9: No match to SDSS)

TABLE 5
CATALOG OF CANDIDATE PERIODIC VARIABLE STARS. II: AOVHARM EPD

ID	P _e ^a d	SN _e ^a	Amp _{eeI} ^b mag	Amp _{eeR} ^b mag	Amp _{etI} ^b mag	Amp _{etR} ^b mag	Q _e ^c
HAT-086-0001701	-99.999999	-999.99	-9.999	-9.999	-9.999	-9.999	2
HAT-086-0004017	40.868328	95.12	-9.999	0.014	-9.999	0.011	1
HAT-086-0005153	16.368924	49.27	-9.999	0.010	-9.999	0.003	0
HAT-086-0005542	20.363047	64.94	-9.999	0.010	-9.999	0.009	0
HAT-086-0005602	-99.999999	-999.99	-9.999	-9.999	-9.999	-9.999	2
HAT-086-0006520	11.462731	64.66	-9.999	0.024	-9.999	0.005	0
HAT-086-0008187	-99.999999	-999.99	-9.999	-9.999	-9.999	-9.999	2
HAT-086-0009482	13.561425	42.66	-9.999	0.018	-9.999	0.009	0
HAT-086-0011792	79.872558	106.96	-9.999	0.022	-9.999	0.002	1
HAT-086-0013793	11.341684	38.88	-9.999	0.012	-9.999	0.005	0
...							

^a The subscript denotes the light-curve type (e: EPD, t: TFA).

^b The peak-to-peak amplitude. The first letters in the subscript denotes the period used, the second letter in the subscript denotes the light-curve type used to calculate the amplitude (e: EPD, t: TFA), the last letter denotes the filter (I or R).

^c Quality flag (0: robust detection, 1: questionable detection, 2: not detected by the given method for the given light curve type).

TABLE 6
CATALOG OF CANDIDATE PERIODIC VARIABLE STARS. III: AoVHARM TFA

ID	P _t ^a d	SN _t ^a	Amp _{teI} ^b mag	Amp _{teR} ^b mag	Amp _{tt} ^b mag	Amp _{tR} ^b mag	Q _t ^c
HAT-086-0001701	17.887814	41.17	-9.999	0.010	-9.999	0.005	0
HAT-086-0004017	-99.999999	-999.99	-9.999	-9.999	-9.999	-9.999	2
HAT-086-0005153	-99.999999	-999.99	-9.999	-9.999	-9.999	-9.999	2
HAT-086-0005542	20.411745	29.90	-9.999	0.010	-9.999	0.009	0
HAT-086-0005602	21.071980	47.14	0.019	0.016	0.010	0.009	1
HAT-086-0006520	11.503656	20.59	-9.999	0.024	-9.999	0.007	0
HAT-086-0008187	5.358132	22.44	-9.999	0.029	-9.999	0.018	0
HAT-086-0009482	-99.999999	-999.99	-9.999	-9.999	-9.999	-9.999	2
HAT-086-0011792	-99.999999	-999.99	-9.999	-9.999	-9.999	-9.999	2
HAT-086-0013793	-99.999999	-999.99	-9.999	-9.999	-9.999	-9.999	2
...							

^a The subscript denotes the light-curve type (e: EPD, t: TFA).

^b The peak-to-peak amplitude. The first letters in the subscript denotes the period used, the second letter in the subscript denotes the light-curve type used to calculate the amplitude (e: EPD, t: TFA), the last letter denotes the filter (I or R).

^c Quality flag (0: robust detection, 1: questionable detection, 2: not detected by the given method for the given light curve type).

TABLE 7
CATALOG OF CANDIDATE ECLIPSING BINARIES. I: ASTROMETRIC AND PHOTOMETRIC DATA

ID	RA ^a h:m:s	DE ^a deg:m:s	pmRA ^b mas/yr	pmDE ^b mas/yr	Jmag ^c mag	Hmag ^c mag	Kmag ^c mag	Vmag mag	Vref ^d	Nnbr ^e	Bl1 ^f	Bl2 ^f
HAT-086-0022206	23:50:17.08	+51:11:28.9	37.45	-20.48	11.655	11.009	10.858	13.656	1	5	1	9
HAT-087-0016301	00:34:50.23	+53:42:12.1	-37.41	12.76	11.310	10.613	10.433	13.904	2	5	2	9
HAT-088-0017192	01:38:56.50	+48:52:40.2	-11.17	-29.81	11.469	10.807	10.608	13.920	1	2	0	1
HAT-113-0005699	18:09:47.63	+49:02:55.0	-53.66	-21.85	11.362	10.710	10.560	14.126	1	1	0	9
HAT-127-0008153	03:04:05.20	+42:03:10.5	53.86	-54.80	10.650	9.983	9.730	14.159	1	2	2	9
HAT-127-0009895	03:02:22.68	+43:40:48.0	-76.01	-30.99	11.018	10.375	10.198	13.890	1	5	3	9
HAT-129-0025342	04:13:06.81	+41:21:01.4	42.67	-26.33	11.938	11.372	11.160	14.311	1	1	1	9
HAT-131-0026711	05:16:36.90	+48:35:44.3	-14.58	-32.73	11.802	11.138	10.982	14.275	1	5	1	9
HAT-132-0012475	05:43:20.18	+47:17:00.1	7.93	-29.15	11.345	10.704	10.569	13.765	1	1	2	9
HAT-133-0001901	06:31:57.29	+41:33:57.3	-56.65	-45.10	9.581	8.930	8.787	11.638	1	2	1	9
...												

^a J2000, from 2MASS

^b from PPMX

^c from 2MASS

^d Source for Vmag (0: PPMX (Tycho-2), 1: Transformed from USNO-B1.0, 2: Transformed from 2MASS)

^e Number of other 2MASS sources within 30''

^f Blending Flag, Bl1 is determined from 2MASS, Bl2 is determined from SDSS (0: unblended, 1: unlikely blend, 2: possible blend, 3: probable blend, 9: no match to SDSS)

TABLE 8
CATALOG OF CANDIDATE ECLIPSING BINARIES. II: EPHEMERIDES

ID	Per d	ePer d	HJD0p ^a d	eHJD0p ^b d	DURp ^c h	HJD0s ^a d	eHJD0s ^b d	DURs ^c h
HAT-086-0022206	0.4290339	0.0000062	2454431.11547	0.00042	1.53	2454436.90565	0.00117	1.52
HAT-087-0016301	3.1325961	0.0003763	2454427.60691	0.00504	5.24	2454416.64515	0.00442	4.63
HAT-088-0017192	1.4030920	0.0000252	2453693.67973	0.00066	2.15	2453680.35434	0.00071	2.00
HAT-113-0005699	0.2278737	0.0000013	2453901.88979	0.00028	1.24	2453905.42128	0.00039	1.14
HAT-127-0008153	2.5681924	0.0000869	2452979.53695	0.00140	1.98	2452991.10638	0.00215	1.53
HAT-127-0009895	0.5916726	0.0000239	2452985.85734	0.00187	4.16	2452990.88691	0.05334	4.55
HAT-129-0025342	4.6109145	0.0002340	2453726.54374	0.00129	2.85	2453724.34418	0.00235	3.34
HAT-131-0026711	0.6639531	0.0000048	2454497.17095	0.00026	1.43	2454498.83198	0.00170	1.42
HAT-132-0012475	0.8663223	0.0000035	2454128.11503	0.00145	3.12	9999999.99999	9.99999	9.99
HAT-133-0001901	0.2929328	0.0000001	2453390.29599	0.00016	0.91	2453376.38208	0.00022	0.88
...								

^a Epoch of primary (p) or secondary (s) eclipse. The value is 9999999.99999 if a secondary eclipse is not detected.

^b Uncertainty on the epoch of eclipse.

^c Eclipse duration.

TABLE 9
CATALOG OF FLARE EVENTS. I: ASTROMETRIC AND PHOTOMETRIC DATA^a

ID	RA ^b h:m:s	DE ^b deg:m:s	pmRA ^c mas/yr	pmDE ^c mas/yr	Jmag ^d mag	Hmag ^d mag	Kmag ^d mag	Vmag mag	Vref ^e
HAT-087-0002617	00:21:57.81	+49:12:38.0	205.00	-32.56	9.139	8.454	8.205	12.474	1
HAT-094-0007885	05:35:22.84	+53:16:02.7	4.39	-35.34	10.797	10.139	9.958	13.797	1
HAT-101-0000851	09:59:39.19	+48:47:54.6	-45.67	8.38	9.686	9.002	8.817	12.137	1
HAT-103-0001602	11:03:17.04	+49:48:25.5	-63.32	-7.74	10.898	10.286	10.114	13.544	1
HAT-119-0031226	22:02:08.40	+49:07:17.3	-68.41	0.39	11.102	10.434	10.228	12.777	1
HAT-123-0002064	00:53:06.48	+48:29:38.5	220.82	-162.32	9.427	8.773	8.580	12.899	0
HAT-123-0002064	00:53:06.48	+48:29:38.5	220.82	-162.32	9.427	8.773	8.580	12.899	0
HAT-123-0003289	00:41:41.41	+44:10:53.1	-46.23	-15.14	10.012	9.399	9.188	14.251	1
HAT-126-0002065	02:40:52.51	+44:52:36.5	215.74	3.85	9.277	8.696	8.461	13.197	0
HAT-128-0007422	03:42:45.17	+43:27:40.1	30.96	-64.10	10.435	9.830	9.568	14.611	1
...									

^a Stars may be listed more than once if they have multiple flare events

^b J2000, from 2MASS

^c from PPMX

^d from 2MASS

^e Source for Vmag (0: PPMX (Tycho-2), 1: Transformed from USNO-B1.0, 2: Transformed from 2MASS)

TABLE 10
CATALOG OF FLARE EVENTS. II: FLARE DATA^a

ID	HJD ^b d	Amp ^c	τ ^d d	Nobs ^e
HAT-087-0002617	2454437.61429	0.130	0.0047	26
HAT-094-0007885	2454463.88452	0.219	0.0092	7
HAT-101-0000851	2454162.63179	0.200	0.0176	26
HAT-103-0001602	2454563.96193	0.279	0.0212	29
HAT-119-0031226	2453360.74326	0.552	0.0346	31
HAT-123-0002064	2454337.05672	0.118	0.0053	11
HAT-123-0002064	2454391.64587	0.482	0.0065	15
HAT-123-0003289	2454338.90758	0.236	0.0087	23
HAT-126-0002065	2452999.82533	0.277	0.0056	9
HAT-128-0007422	2453387.68872	0.346	0.0216	13
...				

^a Stars may be listed more than once if they have multiple flare events

^b Time of flare peak

^c Peak intensity relative to the non-flaring intensity.

^d 1/e decay time of the flare.

^e Number of observations included in fitting the flare.

TABLE 11
CROSS-MATCHES TO PREVIOUSLY IDENTIFIED VARIABLE STARS

ID	Alternate ID	Mflag ^a	BIFlag1 ^b	BIFlag2 ^b
HAT-086-0005602	V0544 Cas	1	3	9
HAT-086-0022206	V1001 Cas	0	1	9
HAT-091-0010976	V0524 Per	0	2	9
HAT-091-0016338	V0485 Per	0	1	9
HAT-112-0001188	1SWASP J173659.28+485946.1	0	0	9
HAT-128-0006973	NSV 01380	1	3	9
HAT-128-0022221	EZ Per	1	3	9
HAT-141-0000663	BT UMa	0	0	0
HAT-144-0000282	1SWASP J132712.10+455826.4	0	0	1
HAT-144-0000526	DE CVn	0	0	1
...				

^a 0: the match is correct, 1: the two stars are not the same, but may be blended in the HAT images.

^b Automatically generated blending flag. BIFlag1 is determined from 2MASS, BIFlag2 is determined from SDSS. 0: unblended, 1: unlikely blend, 2: potential blend, 3: probable blend, 4: source is a flare star, no blending info is generated, 9: no SDSS match.

TABLE 12
CROSS-MATCHES TO ROSAT X-RAY SOURCES

ID	RosatID ^a	lgfxfj ^b
HAT-087-0001873	1RXS J002854.1+502226	-1.7955
HAT-087-0002547	1RXS J003633.7+553728	-2.2528
HAT-087-0002617	1RXS J002158.0+491245	-2.1767
HAT-093-0001111	1RXS J044853.2+552725	-2.3278
HAT-094-0004894	1RXS J050718.8+530713	-2.3805
HAT-094-0005389	1RXS J053001.7+484932	-2.0147
HAT-094-0006428	1RXS J050809.3+532437	-1.7462
HAT-094-0009460	1RXS J050012.4+532033	-1.6652
HAT-094-0384094	1RXS J053625.1+533618	-2.2575
HAT-103-0001602	1RXS J110318.0+494822	-1.8031
	...	

^a ID of matching ROSAT source

^b Estimated $\log(f_x/f_J)$ (ratio of X-ray flux to J-band flux).